Examining Internal and External Contributors to Greenland Climate Variability Using CCSM3

HEATHER J. ANDRES AND W. R. PELTIER

Department of Physics, University of Toronto, Toronto, Ontario, Canada

(Manuscript received 30 November 2012, in final form 1 August 2013)

ABSTRACT

Greenland climate variability is connected to internal and external sources of global climate forcing in six millennium simulations using Community Climate System Model, version 3. The external forcings employed are consistent with the protocols of Paleoclimate Modelling Intercomparison Project Phase 3. Many simulated internal climate modes are characterized over the years 850–1850, including the Atlantic meridional overturning circulation (AMOC), the Atlantic multidecadal oscillation (AMO), the east Atlantic pattern (EA), the El Niño–Southern Oscillation, the North Atlantic Oscillation (NAO), the North Atlantic sea ice extent, and the Pacific decadal oscillation (PDO). Lagged correlation and multivariate regression methods connect Greenland temperatures and precipitation to these internal modes and external sources of climate variability.

Greenland temperature and precipitation are found to relate most strongly to North Atlantic sea ice extent, the AMO, and the AMOC, that are themselves strongly interconnected. Furthermore, approximately half of the multidecadal variability in Greenland temperature and precipitation are captured through linear relationships with volcanic aerosol optical depth, solar insolation (including total solar irradiance and local orbital variability), the NAO, the EA, and the PDO. Relationships are robust with volcanic aerosol optical depth, solar insolation, and an index related to latitudinal shifts of the North Atlantic jet. Differences attributable to model resolution are also identified in the results, such as lower variability in the AMOC and Greenland temperature in the higher-resolution simulations. Finally, a regression model is applied to simulations of the industrial period to show that natural sources alone only explain the variability in simulated Greenland temperature and precipitation up to the 1950s and 1970s, respectively.

1. Introduction

Since the late 1990s, global and regional climate reconstructions and simulations have been employed to isolate the contributions from internal climate modes and external forcings to climate variability over millennial time scales. In particular, many studies focus on how unusual global temperature changes over the past century are in the historical context of global or hemispheric temperature variability (Frank et al. 2010). However, separating the roles of external forcings, such as solar variations and volcanoes, in generating multidecadal climate variability over the preindustrial millennium has also been a primary focus (Crowley 2000; Goosse et al. 2005; Ammann et al. 2007; Jungclaus et al. 2010), as it is important for the purpose of isolating the climate effects of greenhouse gases and aerosols since the industrial revolution. For example, Ammann et al. (2007) show that, although forcing simulations with varying amplitudes of multidecadal total solar irradiance variability generate different global temperatures over the past millennium, anthropogenic forcings are required to reproduce observed temperature increases after 1940 (Ammann et al. 2007).

Our study employs millennium-length simulations to examine the connections between elements of Greenland ice sheet (GrIS) mass balance and both natural external forcings (solar insolation and volcanic eruptions) as well as internal sources of variability in the North Atlantic [including the North Atlantic Oscillation (NAO), the east Atlantic pattern (EA), the Pacific decadal oscillation (PDO), the El Niño–Southern Oscillation (ENSO), North Atlantic sea ice extent, the Atlantic multidecadal oscillation (AMO), and the Atlantic meridional overturning circulation (AMOC)]. Previous analyses suggest that internal modes can be an important source of temperature variability in the North

Corresponding author address: Heather Andres, Department of Physics, University of Toronto, 60 St. George St., Toronto ON M5S 1A7, Canada.
E-mail: handres@atmosp.physics.utoronto.ca

DOI: 10.1175/JCLI-D-12-00845.1

Atlantic over the past millennium and that natural external forcings can affect North Atlantic modes of variability on multidecadal time scales (Tett et al. 2007; Hegerl et al. 2011; Swingedouw et al. 2011). Thus, in order to extract the separate roles of both internal and external climate forcings in generating North Atlantic climate variability, we employ a modern coupled atmosphere–ocean general circulation model to construct a ''mini ensemble'' of six millennium time-scale simulations. We provide detailed analyses of the connections between the time scales of North Atlantic climate variability and those associated with natural modes of climate fluctuations and external climate forcings in this model. Our study provides a strong foundation for commenting on the role of anthropogenic forcings on Greenland temperatures and precipitation in the industrial-era simulations that have also been performed using this model.

Understanding the responses of Greenland temperature and precipitation to anthropogenic forcings is crucial, since both the GrIS and the West Antarctic ice sheet (WAIS) have already moved from a state of relative mass balance to one of significant mass imbalance over the past 20 years (Velicogna and Wahr 2006; Alley et al. 2007; Peltier 2009; Shepherd et al. 2012). Furthermore, Miller et al. (2012) suggest that sea levels were approximately 22 $\pm$ 5 m higher than present under carbon dioxide concentrations very close to modern levels ($\sim$400 ppmv) during the mid-Pliocene, 3 million years before present. Global average temperatures in that period are also inferred to have been 2°–3°C warmer than present. A rise in sea level of that magnitude requires not only the total elimination of both the GrIS and the WAIS but also significant mass loss from at least the periphery of the East Antarctic ice sheet. In the future, meltwater generated by the retreat of continental-scale ice sheets, as well as small ice caps and glaciers, will again undoubtedly be a dominant contributor to sea level rise. Given that approximately 38% of the global population lives within 20 km of a coast and at an elevation less than 20 m above mean sea level (Small and Nicholls 2003), rising global sea levels constitute an important consequence of anthropogenically driven climate change.

Numerous analyses indicate that the rate of mass loss from the GrIS has been accelerating over the past decade [e.g., for a review, see Alley et al. (2010)]. Current understanding suggests that the causes of this acceleration have been equally divided between increased flow of outlet glaciers at the margins of the ice sheet and increased meltwater runoff from the ice sheet surface (van den Broeke et al. 2009). It is also possible that surface meltwater runoff may be driving some of the dynamical changes, although Schoof (2010) suggests that any dynamic responses to surface melt variability are short lived. These mass balance changes have occurred concurrently with temperature increases over the ablation zone and precipitation increases over the interior of the ice sheet (Hanna et al. 2008). Such relatively high temperatures and consequent increase in GrIS mass loss have been commonly understood as components of polar amplification of anthropogenically induced climate change (e.g., Masson-Delmotte et al. 2006). However, in order to validate this claim, we require an accurate characterization of the amplitudes and time scales of natural fluctuations in Greenland surface conditions, including both temperature and precipitation. For example, both Hanna et al. (2008) and Fettweis et al. (2011) find that Greenland melt responds strongly to the NAO, although an even stronger association is found with local high pressure blocking over Greenland through the Greenland blocking index (Hanna et al. 2013). Station measurements have also shown that temperatures increased over many sites along the Greenland coast from the 1920s until the 1930s (Chylek et al. 2006; Box et al. 2009; Wake et al. 2009), which is a period of warming understood to have been most probably driven by natural variability (Delworth and Mann 2000; Ammann et al. 2007). Properly attributing the causes of recent and past Greenland mass balance changes will be crucial to enabling probabilistically accurate predictions of Greenland mass loss in the future as greenhouse gas–induced warming continues.

The primary agents of North Atlantic climate variability are thought to include volcanic aerosols, the NAO, and sea ice–ocean feedbacks (Hanna et al. 2005; Fettweis 2007; Hanna et al. 2008; Box et al. 2009; Schneider et al. 2009; Frauenfeld et al. 2011; Miller et al. 2012). Other natural factors are also hypothesized to influence Greenland mass balance, including sea ice distributions (Hanna et al. 2009), changes in heat transport from the equator to the pole (Box et al. 2009), atmospheric circulation changes associated with solar variability (Box et al. 2009), and sea surface temperature (SST) variations in the North Atlantic ocean immediately adjacent to Greenland (Hanna et al. 2009).

Volcanic eruptions have been demonstrated to decrease Greenland temperatures and reduce runoff during the twentieth century in both reanalysis products and regional models (Hanna et al. 2005; Box et al. 2009). Hanna et al. (2005) show that positive Greenland surface mass balance values follow years of volcanic eruptions in European Centre for Medium-Range Weather Forecasts (ECMWF) data, resulting from runoff reductions concurrent with unaffected accumulation. Box et al. (2009) conclude, based on analyses with the polar version

of the fifth-generation Pennsylvania State University–National Center for Atmospheric Research Mesoscale Model (Polar-MM5), that Greenland temperatures are more than three standard deviations colder than their climatological average in years during volcanic eruptions. This cooling is found to be strongest over western Greenland and during winter.

The connections between Greenland temperatures and precipitation and the NAO have proven less robust. They are sensitive to the period (Hanna et al. 2008), the season (Fettweis 2007; Hanna et al. 2008; Frauenfeld et al. 2011) and the region of Greenland examined (Fettweis 2007; Frauenfeld et al. 2011). For example, Hanna et al. (2008) find significant negative correlations between Greenland average summer temperatures obtained from Greenland climate stations and an NAO summer index from 1961 to 1991. However, after 1991, the strength of these correlations decreases. Fettweis (2007) employs a regional climate model to argue that temperatures over all of the GrIS are negatively correlated with the usual winter NAO index but only during winter and predominantly in the southwest sector of the ice sheet. Similarly, Frauenfeld et al. (2011) demonstrate that, from 1979 to 2009, the winter NAO index is significantly related to total annual GrIS melt extent, although not through relationships with summer temperatures on the southern coasts of Greenland, where most of the melt occurs. Precipitation responses to the NAO are characterized by even more regional variability (Fettweis 2007). Fettweis (2007) shows that precipitation is anticorrelated with the winter NAO index on the western and southeastern coasts, particularly during fall and winter, and positively correlated on the northeastern coast, particularly during summer and fall. These patterns are consistent with the low pressure center of the positive NAO being located northeast of Greenland, as shown in Fig. 1, which is discussed below. Overall, Fettweis (2007) finds that the NAO does not correlate with annual precipitation averaged over the entire ice sheet and attributes changes in average annual precipitation to other causes, in particular to increasing greenhouse gas concentrations.

The roles of sea ice–ocean feedbacks are even more difficult to identify, since their interactions are complex and can involve many other processes in the North Atlantic. Different climate models appear to favor different mechanisms of interrelation between the NAO, the AMOC, the AMO, and North Atlantic sea ice (see a review in Grossmann and Klotzbach 2009; Danabasoglu 2008; d'Orgeville and Peltier 2009b; Escudier et al. 2013; Swingedouw et al. 2013), although some consistencies are present. For example, models in the Intergovernmental Panel on Climate Change (IPCC) Fourth Assessment Report (AR4) indicate that the AMOC leads and is strongly correlated with the AMO (Medhaug and Furevik 2011). Observational studies are of limited usefulness for discriminating between these different mechanisms because of the multidecadal time scales of the interactions and the limited datasets available for these variables (Danabasoglu et al. 2012; Swingedouw et al. 2013). Time scales of the interaction processes generally fall either between 20 and 30 yr or between 50 and 100 yr (d'Orgeville and Peltier 2009b; Danabasoglu et al. 2012; Escudier et al. 2013; Swingedouw et al. 2013), and the Community Climate System Model, version 3 (CCSM3), has exhibited AMOC variability in each of these categories (Danabasoglu 2008; d'Orgeville and Peltier 2009b). Danabasoglu (2008) identifies a 21-yr oscillation in AMOC variability that is triggered equally by temperature and salinity variations at the site of deep-water formation in the Labrador Sea. The temperature and salinity variations are attributed to changes in the strength of the subpolar gyre circulation, which responds to variations in the NAO (Danabasoglu 2008). Sea ice is forced in opposite ways by the NAO and the AMOC and influences the phasing of the AMOC oscillation (Danabasoglu 2008). In contrast, d'Orgeville and Peltier (2009b) identify a 60-yr periodicity in the AMOC from another set of CCSM3 simulations. In their runs, the AMOC responds primarily to salinity changes caused by barotropic circulation interactions with the bottom bathymetry (d'Orgeville and Peltier 2009b). They note that the NAO may play a more subsidiary role in generating AMOC variability (d'Orgeville and Peltier 2009b). Thus, Greenland temperatures and precipitation are likely connected to many climate processes in the North Atlantic through complex interactions and disentangling their separate contributions is a challenge. Nevertheless, sea ice variability has previously been demonstrated to play an important role in driving large amplitude changes in inferred temperatures from ice cores at Summit, Greenland during the Younger–Dryas event (Tarasov and Peltier 2005; Peltier et al. 2006).

Other studies employ model simulations to analyze the roles of internal climate variability in generating regional and global temperature variability in the period prior to extensive observational records being available (Tett et al. 2007; Hegerl et al. 2011; Swingedouw et al. 2011). Two challenges for accurately characterizing past climate variability using model simulations are that the results depend first on the ability of the model to characterize the modes of natural climate variability well and second on the accuracy of model forcing reconstructions over the target period. Furthermore, it is assumed that the structures of the natural climate modes do not change in response to the forcing.

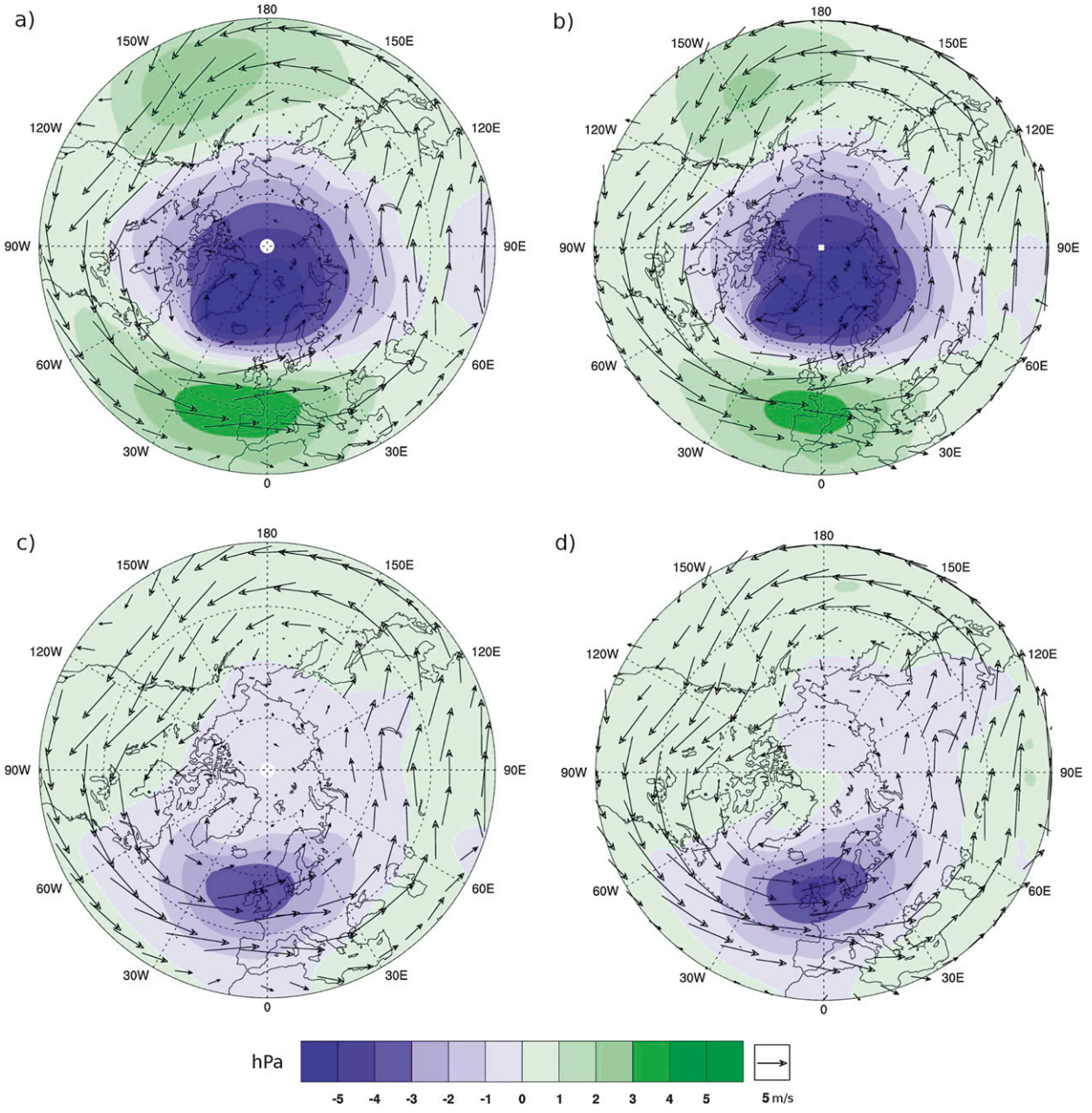

FIG. 1. Projections of the (a),(b) NAO and (c),(d) EA onto Northern Hemisphere sea level pressures (hPa) for (a),(c) T42 and (b),(d) T85 simulations. Superimposed over these contours are climatological wind vectors ($m\,s^{-1}$) for DJF from the corresponding simulations.

Hegerl et al. (2011) employ both models and observations to identify significant signatures of external climate forcings in European temperatures during winter and spring from 1500 to 1996. They create estimates of internal climate variability over this period by regressing a historical temperature reconstruction against templates of European climate responses to a number of sources of internal and external variability obtained from three previously published atmosphere–ocean GCM (AOGCM) millennium runs. They then examine the residuals for signatures of external forcings and obtain robust responses to volcanic and anthropogenic forcings. This method treats internal and external climate forcings as independent, even though external forcings may project onto internal modes of variability. Tett et al. (2007) show that the NAO exhibits no change in behavior when natural and anthropogenic forcings are included in Hadley Centre Coupled Model, version 3

(HadCM3), simulations as compared to a control run. On the other hand, the AMOC shows a modest increase in multidecadal variability. In general, Tett et al. (2007) demonstrate that North Atlantic temperatures and sea ice cover respond more strongly to anthropogenic forcings than to natural forcings, particularly on multidecadal time scales. On the other hand, Swingedouw et al. (2011) identify significant responses in both the simulated NAO and AMOC to total solar irradiance forcing, with time lags of 40 and 10 yr, respectively. In particular, they note that from 1750 to 1800 the NAO index in their single simulation deviates negatively from its mean value (Swingedouw et al. 2011). They suggest that this may be a delayed response to the solar Maunder Minimum, although Swingedouw et al. (2011) point to the need for more ensemble members in order to validate connections over this time period.

2. Design of the ensemble of numerical simulations

Our analyses of the controls on Greenland ice sheet mass balance are based on a mini ensemble of six millennium time-scale climate simulations. These simulations span the last 1000 years of the preindustrial period and are extended into the instrumental era, when anthropogenic warming of the lower atmosphere has occurred. Our goal is to employ the results from this ensemble to separate the anthropogenic signal from natural variability. To this end, we have produced this set of six long simulations to explore the nature of multidecadal components of natural internal variability in the North Atlantic, as it is variability on these time scales that can most effectively obscure the response of the GrIS to anthropogenic climate change. We chose to simulate the period 850–1850, because it covers a sufficiently recent era that we expect the natural climate regime to be similar to that of the present day. This is expected to contrast sharply with the subsequent ''Anthropocene'' when greenhouse warming has come to dominate.

a. The numerical model and the design of the millennium-time-scale experiments

For all our simulations, we employ CCSM3, which is a fully coupled atmosphere–ocean general circulation model developed by the National Center for Atmospheric Research (NCAR) (Collins et al. 2006). This model was run with fully interactive components for the atmosphere, land surface, sea ice, and oceans. The atmospheric and land components consist of Eulerian spectral dynamical cores operating on a shared Gaussian grid, and the ocean and sea ice components each apply finite difference methods on a shared grid with the north pole displaced to a position over Greenland (Collins et al. 2006). The model resolutions chosen for this study represent a compromise between the need for high resolutions over Greenland in order to capture regional distributions of temperature and precipitation and low enough resolution to enable multiple millennium-length global simulations to be performed within the limits imposed by available computational resources. Given these constraints, we have elected to create six transient simulations, including three at an atmospheric spectral resolution of T42 and three at a resolution of T85. T42 and T85 are the two highest spectral resolutions available for the atmospheric model and correspond to roughly 2.8° × 2.8° and 1.4° × 1.4°, respectively, in horizontal resolution (Collins et al. 2006). Both resolutions of the atmospheric model have 26 vertical levels on a hybrid coordinate (Collins et al. 2006) that reaches an altitude of 3.5 hPa. The ocean and sea ice components are identical in all simulations and share a grid roughly equivalent to 1° in longitude with variable latitudinal resolution that corresponds roughly to 0.5° (Collins et al. 2006).

Separate control runs for each resolution were independently equilibrated to boundary conditions for the year 850. They were both initialized from partially equilibrated 1870 control runs, although the T85 sea ice and ocean components were initialized from the lower-resolution 850 control run after it had completed part of its equilibration process. The equilibration criteria were decided upon following analyses of the adjustment time scales present during the equilibration process and are conservative compared to previous work (Hack et al. 2006). They are first for globally averaged surface temperatures and top-of-model net radiation fluxes to be without significant trends for at least 200 years, and second for the top-of-model net radiation fluxes to be within $\pm 0.1\,\mathrm{W\,m^{-2}}$. The equilibration process required 2090 and 1300 simulation years for the T42 and T85 resolutions, respectively, after which the control runs were continued for a further 1000 simulation years. The equilibration criteria are found to be effective, as the T42 (T85) control run exhibits least squares–minimized linear trends in both globally averaged surface temperatures and top-of-model net radiation fluxes of $-0.03^{\circ}\mathrm{C\,ka^{-1}}$ ($-0.07^{\circ}\mathrm{C\,ka^{-1}}$) and $0.02\,\mathrm{W\,m^{-2}\,ka^{-1}}$ ($0.03\,\mathrm{W\,m^{-2}\,ka^{-1}}$), respectively, following equilibration. Furthermore, both control simulations exhibit mean top-of-model net radiation fluxes of $-0.07\,\mathrm{W\,m^{-2}}$ following the equilibration procedure, where positive indicates a downward flux. All transient simulations at a given resolution were initialized from the same year in their corresponding control run and were run from year 850 to 1850, although because of irretrievable loss not all of these data are available.

TABLE 1. List of numerical simulations used in these analyses with their characteristics.

Name	Resolution	Dates		Orbital	Volcanic	Solar	Trace gases	Aerosols
		Start	End					
Mill_T42_ctl	T42	2940	3940	Fixed	Fixed	Fixed	Fixed	Fixed
Mill_T85_ctl	T85	2150	3150	Fixed	Fixed	Fixed	Fixed	Fixed
Mill_T42_all_Gao	T42	932	1850	Transient	Gao	Transient	Transient	Fixed
Mill_T42_all_Crowley	T42	850	1850	Transient	Crowley	Transient	Transient	Fixed
Mill_T42_sol_Gao	T42	850	1850	Transient	Gao	Transient	Fixed (850)	Fixed
Mill_T85_all_Gao	T85	1000	1850	Transient	Gao	Transient	Transient	Fixed
Mill_T85_all_Crowley	T85	1100	1850	Transient	Crowley	Transient	Transient	Fixed
Mill_T85_all_Crowley2	T85	850	1850	Transient	Crowley	Transient	Transient	Fixed
Ind_T42_all_Gao	T42	1850	2000	Transient	Gao	Transient	Transient	Transient
Ind_T42_all_Crowley	T42	1850	2000	Transient	Crowley	Transient	Transient	Transient
Ind_T42_sol_Gao	T42	1850	2000	Transient	Gao	Transient	Fixed (1850)	Fixed
Ind_T85_all_Gao	T85	1850	2000	Transient	Gao	Transient	Transient	Transient
Ind_T85_all_Crowley	T85	1850	2000	Transient	Crowley	Transient	Transient	Transient
Ind_T85_all_Crowley2	T85	1850	2000	Transient	Crowley	Transient	Transient	Transient

Industrial simulations were then initialized from the end points of each of the millennium simulations and run to year 2000. The set of six model simulations provides the basis for all of our analyses presented below.

Forcing fields provided to the model include greenhouse gas concentrations, ozone concentrations, volcanic aerosol masses, total solar irradiance, aerosol mass mixing ratios and orbital configuration. All of the preindustrial simulations were forced with the same ozone and aerosol climatologies, and total solar irradiance and orbital time series. All but one of the preindustrial simulations were forced with time-varying greenhouse gas concentrations. In the remaining T42 simulation, greenhouse gas concentrations were held fixed at year 850 values. Finally, two volcanic forcing reconstructions were employed. All of the industrial simulations were forced with the same ozone, total solar irradiance, and orbital configuration time series. Modifications were made by the authors to the CCSM3 source code in order to allow time-varying prescribed aerosol masses. All but one of the simulations employed time-varying greenhouse gas concentrations and aerosol masses, while the remaining T42 simulation held them fixed at year 1850 conditions. Again, the same two volcanic reconstructions were employed over this time period. An outline of the differences between the simulations is provided in Table 1. Further descriptions of the forcing datasets are provided below. Note that Mill_T85_all_Crowley and Mill_T85_all_Crowley2 simulations are forced identically from the same initialization point, but they are not the same because of updates to the supercomputer software available at their run times.

Preindustrial datasets were specified consistent with the Paleoclimate Modelling Intercomparison Project Phase 3 (PMIP3) last-millennium experiment as described in Schmidt et al. (2012). Industrial simulation datasets were consistent with phase 5 of the Coupled Model Intercomparison Project (CMIP5) historical experiment where possible (CMIP5 2011).

The datasets employed to specify the volcanic aerosol forcing history are those from Gao et al. (2008) in units of mass and Crowley et al. (2008) in units of aerosol optical depth (AOD). Volcanic reconstructions over this period depend on ice core data that have limited spatial information and dating uncertainties (Gao et al. 2008). Consequently, other data sources are employed to infer global aerosol distributions, including observations of recent events and simulations of volcanic aerosol dispersal (Gao et al. 2008). Similarly, volcanic eruption dates are refined by comparing multiple ice cores and referring to historical accounts (Gao et al. 2008). CCSM3 requires that the volcanic aerosols are specified in terms of their mass distribution. Therefore, aerosol optical depths were converted to mass distributions by inverting the shortwave extinction calculation used internally within the atmospheric component of CCSM3, the Community Atmosphere Model, version 3 (CAM3), to obtain an effective extinction coefficient for the incoming shortwave radiation spectrum specified in the model (Collins et al. 2004). Then, a distribution of total column masses was calculated. An average volcanic vertical profile was taken from the Gao dataset, normalized, and multiplied by the Crowley total column masses in order to create consistent mass distribution fields. This method depends on the assumption that all volcanic eruptions reached the same height. Globally averaged aerosol optical depths are plotted in Fig. 2a as a function of time for both the Crowley and Gao datasets.

The total solar irradiance forcing time series was obtained from N. Krivova (2009, personal communication)

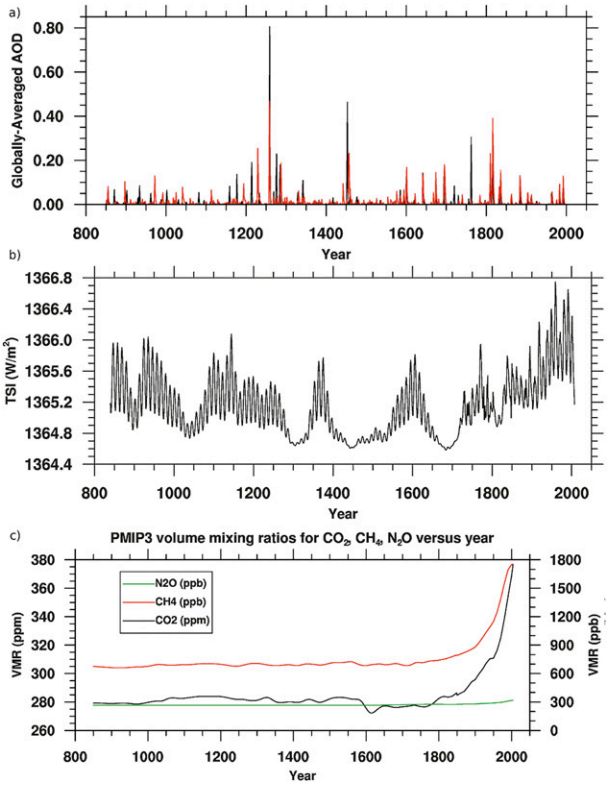

FIG. 2. Forcing data time series employed in the millennium-time-scale simulations. (a) Volcanic aerosol depth averaged over the globe and plotted for Gao et al. (2008) in black and Crowley et al. (2008) in red. (b) Total solar irradiance reconstructed by Vieira et al. (2011). (c) Greenhouse gas forcing time series, with CO_2 in parts per million and CH_4 and N_2O in parts per billion. Data for years 850–1850 are from the PMIP3 specifications, and data for 1850–2005 are from the CMIP5 historical datasets.

for the years 850–2010 and is described in Vieira et al. (2011). Their reconstruction uses different methods for years before and after 1706, as direct observations of sunspot area are only available during the latter period (Krivova et al. 2007). Vieira et al. (2011) estimate the total solar flux as a linear combination of the percentage of the sun's surface filled with sunspots multiplied by average fluxes associated with each one. Their model yields total solar irradiance variations on multicentennial and decadal time scales. For the earlier period, reliable sunspot observations are not available, so sunspot areas are obtained from magnetic open flux measurements reconstructed from records of cosmogenic ^{14}C over cycles spanning each date (Vieira et al. 2011). These records have adequate temporal resolution only on time scales of decades, so Vieira et al. superimpose an artificial 11-yr cycle onto their decadally averaged total solar irradiance reconstructions with a fixed length of 11 yr and an amplitude scaled to the average irradiance value (N. Krivova 2009, personal communication). This total solar irradiance reconstruction yields a difference of 0.1% between the Maunder Minimum and the present day, categorizing it as an irradiance reconstruction with relatively small centennial variations. The time series is plotted in Fig. 2b.

Orbital forcing was incremented in 10-yr time steps, using the Berger (1978) scheme already part of the model code and a code modification developed by B. Briegleb and B. Kauffman (N. Rosenbloom 2009, personal communication). CCSM3 uses orbital forcing as a multiplicative factor with the total solar irradiance to define the solar insolation at the top of the atmosphere. Consequently, we treat the two variables as combined from now on.

Greenhouse gas concentrations varied relatively little over the preindustrial millennium (Schmidt et al. 2012). On the other hand, the CMIP5 historical concentration time series from 1850 to 2000 (Meinshausen et al. 2011) indicate a fast-increasing trend throughout the period. The greenhouse gas concentration time series are shown in Fig. 2c.

Aerosol and ozone concentrations are specified to be climatological at 1850 values in the millennium simulations. Subsequently, they are specified from CMIP5 historical datasets until 2000 (Lamarque et al. 2010). Note that the ozone datasets have been generated assuming emissions of anthropogenic species, so the natural forcing–only industrial run does indirectly include some influence of anthropogenic emissions.

b. Modeled climate biases and resolution differences

CCSM3 exhibits considerable improvements over its predecessor (Collins et al. 2006) and reproduces observed Arctic sea ice declines over the twentieth century better than many other models included in the CMIP3 database (Stroeve et al. 2007). Furthermore, the sea ice component of this model was recently found to be far superior to representations of this climate component in other coupled models during analyses of the ''snowball'' climate of the Neoproterozoic era (Yang et al. 2012a,b). Nevertheless, CCSM3 or CAM3 exhibit biases in the North Atlantic and Arctic regions that may influence the analyses discussed here (deWeaver and Bitz 2006; Holland et al. 2006; Hurrell et al. 2006; Large and Danabasoglu 2006; Higgins and Cassano 2010; Grotjahn et al. 2011).

During December–February (DJF), sea level pressures north of 50°N are lower and sea level pressures in the northern subtropics are higher than corresponding pressures in 40-yr ECMWF Re-Analysis (ERA-40) data (Hurrell et al. 2006; Higgins and Cassano 2010). These biases correspond to anomalously warm Arctic temperatures overall (Grotjahn et al. 2011). Also, the Icelandic low pressure center tends to be too low and too extensive, which is associated with the North Atlantic

storm track being too strong and too zonal. As a consequence, the location of the end of the storm track is shifted southward, so the Barents Sea experiences a positive pressure bias and northern Europe experiences a negative pressure bias (Hurrell et al. 2006; Grotjahn et al. 2011).

The North Atlantic Current is also too zonal, which yields salinity and sea surface temperature biases south of Greenland of up to −4 psu and −10°C, respectively (Large and Danabasoglu 2006). Danabasoglu (2008) note that the sites of largest sea surface temperature and sea surface salinity bias coincide with the regions of highest variability in these variables. Consequently, they suggest that these biases may be responsible for an unrealistic amplitude and pattern of SST variability in the North Atlantic (Danabasoglu 2008).

Overall, Arctic sea ice is too extensive during boreal winter but matches reconstructions during the summer (Holland et al. 2006). The Labrador Sea is too fresh and has excessive winter sea ice cover (Holland et al. 2006; Large and Danabasoglu 2006), while the Barents Sea receives excessive amounts of ocean heat transport and has too little sea ice coverage (Holland et al. 2006). Furthermore, because of the atmospheric circulation biases mentioned above, the distribution of sea ice in the Arctic basin does not match distributions inferred using an offline sea ice model forced by National Centers for Environmental Prediction (NCEP)–NCAR reanalysis data (deWeaver and Bitz 2006). Whereas NCEP–NCAR winds produce sea ice thickness maxima against the Canadian Arctic Archipelago and Greenland coasts, CCSM3 annual sea ice thickness is thickest along the Siberian coast instead (deWeaver and Bitz 2006).

Furthermore, differences in Arctic climate exist depending on the atmospheric and land resolution employed. For example, Arctic sea ice is generally thicker in the T42 configuration than in the T85 configuration, which can be partly explained by the fact that surface air temperatures are roughly 2°C colder across the Arctic in the T42 configuration than the T85 configuration (deWeaver and Bitz 2006; Hack et al. 2006). Also, deWeaver and Bitz (2006) show that only the T85 configuration exhibits any maxima in climatological annual sea ice thickness along the northern coasts of the Canadian Arctic Archipelago and Greenland, in partial agreement with sea ice forced by NCEP–NCAR winds. During the summer, the T42 model configuration actually generates a polar anticyclone of equivalent strength to the polar cyclone found in NCEP–NCAR data, while the T85-resolution model does not exhibit either structure (deWeaver and Bitz 2006). As a result, in both model configurations, less sea ice is rafted against the Canadian and Greenland northern coasts than in reanalysis (deWeaver and Bitz 2006). Finally, less sea ice is exported from the Arctic to the North Atlantic in the T85 configuration than the T42 configuration (deWeaver and Bitz 2006), which implies that there is also less freshwater deposited there.

Large and Danabasoglu (2006) note that the ocean biases in CCSM3 are not affected significantly by increasing the resolution of the atmosphere and land models from T42 to T85. Nevertheless, ocean circulation differences do exist. Namely, Bryan et al. (2006) report that, in present-day control experiments using fully coupled CCSM3, the mean North Atlantic meridional overturning streamfunction is stronger and extends deeper with atmosphere and land components at T85 truncation rather than T42. They demonstrate that the difference in strength is primarily in the secondary formation region between 45° and 50°N, although the locations of the deep-water formation regions are quite similar (Bryan et al. 2006). Bryan et al. (2006) also note that the AMOC exhibits stronger decadal variability in their T85 control simulation than their T42 control. AMOC variability appears suppressed (after detrending) in transient simulations initialized from their control runs at both resolutions, although this suppression is stronger in the T85 simulation. Nevertheless, the T85 variability remains 50% stronger than in the T42 simulation during transient forcing (Bryan et al. 2006). However, during subsequent stabilization experiments initialized from the transient runs, the variability is slightly weaker in the T85 configuration than in the T42 (Bryan et al. 2006).

Grotjahn et al. (2011) note that there are wind biases over Greenland resulting from topography differences between the model and ERA-40 data. We also find that there are resolution differences in the topography of Greenland. Figure 3 shows topographic height contours for Greenland derived from climatological geopotential heights for the (i) T42 and (ii) T85 control runs. Overlaid on these contour plots are the grids employed by each model configuration. Greenland boundaries as defined in these analyses include 115 grid cells in the T42 simulations and 421 grid cells in the T85 simulations. The higher-resolution configuration conforms much more closely to the subcontinent boundaries, yielding a slightly higher total area of 2.45×10^6 versus 2.36×10^6 km^2. Over these same boundaries, the average geopotential heights for Greenland are 1200 m above mean sea level in the low-resolution simulations and 1400 m in the high-resolution runs, with peak heights over 300 m higher in the T85 configuration than in the T42 configuration. These average height differences correspond to approximately 1.5°C difference in mean temperatures based on average lapse rates from the T42 simulations.

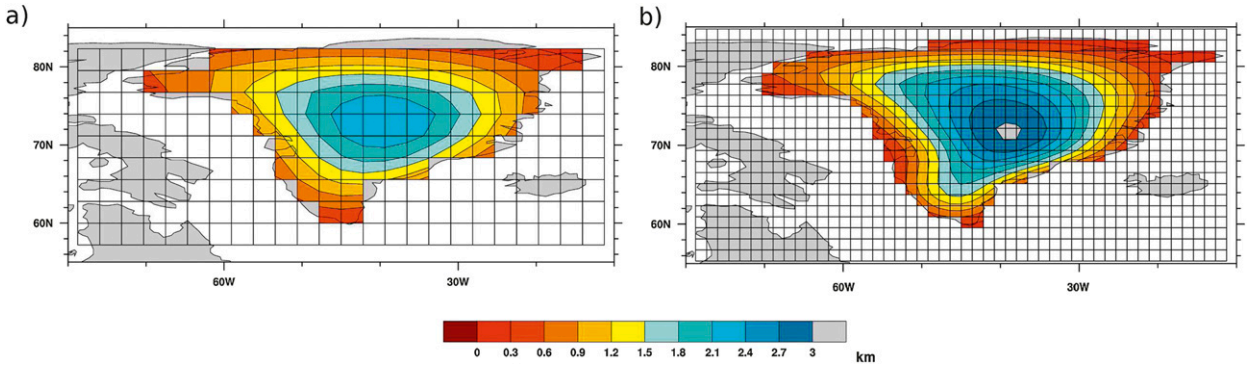

FIG. 3. Greenland topography (km) as determined by climatological surface geopotential heights for the (a) T42 and (b) T85 control runs. Overlaid are the grids used by each of these model configurations.

Finally, precipitation is a difficult process for climate models to capture, since it depends upon convective and cloud-related dynamical processes that extend over a wide range of spatial scales. Consequently, in CCSM3, clouds and precipitation are parameterized and tuned separately for each model configuration (Hack et al. 2006). Large precipitation biases occur, particularly in the intertropical convergence zone and continental subtropics, which affect ocean salinity distributions (Boville et al. 2006; Hack et al. 2006).

c. *Analysis methods used to connect Greenland mass balance variability to other climate indicators*

We have applied multiple linear regression analysis using least squares estimates of the regression parameters to connect Greenland average surface temperatures and Greenland total annual precipitation to various climate indicators. These analyses are performed on annually averaged data smoothed by a Gaussian filter with a half-width of 14 yr. The year in these analyses is defined to start in September and end in August, so that seasons of sea ice growth and melt and Greenland mass balance are kept intact. The year number equals the calendar year of January included in that time period.

Equation (1) shows the multiple linear regression equation applied in this paper for temperatures, where T represents Greenland average annual temperatures,

$$X_T = \beta_{T,\mathrm{volc}} X_{\mathrm{volc}} + \beta_{T,\mathrm{solar}} X_{\mathrm{solar}} + \beta_{T,\mathrm{NAO+EA}} X_{\mathrm{NAO+EA}} + \beta_{T,\mathrm{NAO-EA}} X_{\mathrm{NAO-EA}} + \beta_{T,\mathrm{PDO}} X_{\mathrm{PDO}} + \epsilon. \quad (1)$$

The equation for Greenland total annual precipitation is the same with T replaced by P. The regression parameters are given by $\beta_{T,\_}$, where the second subscript indicates the climate variable being considered. Each climate time series is represented as $X_{T,\_}$ and has been centered and normalized by its standard deviation prior to the regression analysis. The residuals are denoted by ϵ. The regressions were applied to synchronous datasets, except for the volcanic time series, which was lagged by 1 yr. This lag was chosen on the basis of lagged correlation analyses (not shown) and was detected in all the simulations and for both temperature and precipitation.

The variances of the regression parameters are given by

$$\mathrm{var}(\mathbf{b}) = s^2 (X'X)^{-1}, \quad \text{where} \quad s^2 = \sum_{i=1}^{n} \frac{\epsilon_i^2}{n-k} \quad (2)$$

is the variance of the residual terms, and $\mathbf{b}$ is the vector of regression parameters calculated by the model. The term X is the array of predictor variable time series, and $n - k$ represents the effective number of degrees of freedom in the regression calculation. Further details concerning the way in which these values were calculated are presented in the appendix.

The regressions were performed separately for each simulation, and then the regression parameters obtained over the preindustrial period were employed to predict the contribution of natural variability to Greenland climate variability over the industrial period. The differences between this estimate and simulated Greenland conditions allow us to assess whether the anthropogenic signal is separable from natural variability in simulated Greenland conditions during this period.

3. Results

a. *Characterizing global climate in the preindustrial simulations*

We begin these analyses by first presenting comparisons of Northern Hemisphere surface temperature time

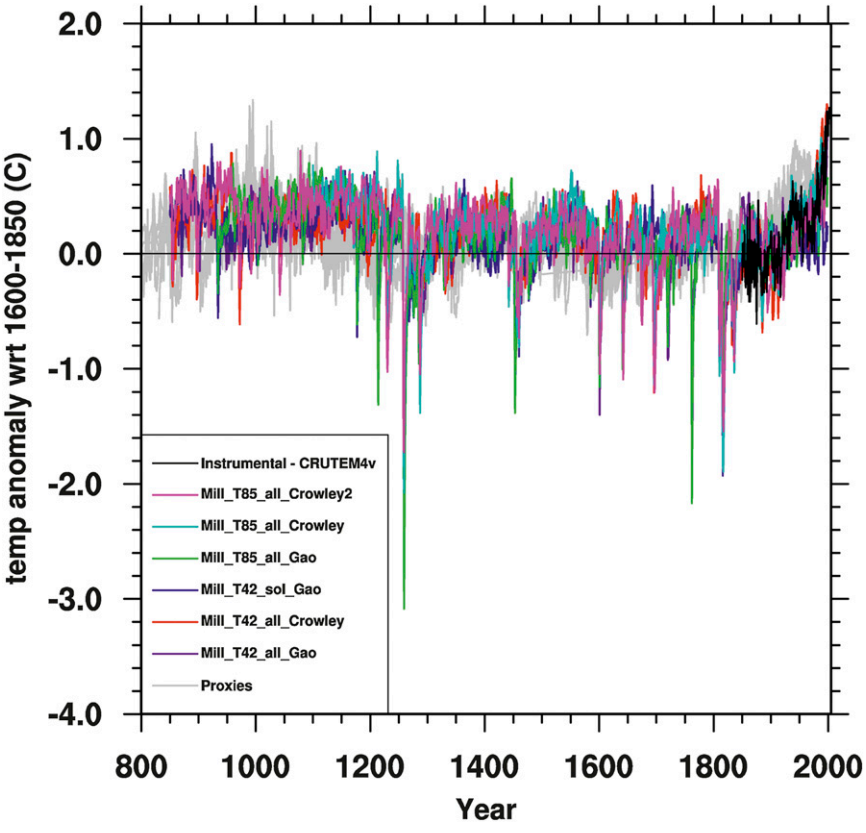

FIG. 4. Northern Hemisphere temperature reconstructions for millennium simulations in colors and IPCC AR4 proxy reconstructions (Jansen et al. 2007) in gray. Instrumental observations are overlain in black, such that their average from 1860 to 1999 equals that of the simulations over that period.

series generated from our simulations with proxy reconstructions available for the preindustrial millennium. Following this discussion, we next introduce the modes of global climate variability examined in this study and characterize their behaviors over this time period.

Time series of annually averaged simulated Northern Hemisphere surface temperature anomalies are plotted for both industrial and preindustrial periods in color in Fig. 4 with proxy reconstruction time series from the IPCC AR4 paleoclimate chapter in gray (Jansen et al. 2007). Temperature anomalies are defined with respect to mean values for each run over the period 1600–1850, which is the longest preindustrial period common to the proxy datasets and simulations. The observational Hadley Centre Climate Research Unit variance-adjusted near-surface air temperature anomalies, version 4 (CRUTEM4v), dataset (Jones et al. 2012) is overlaid in black. Since there are no observational data prior to 1850, its mean over 1860–1999 was defined to equal that of the simulations. The first attribute of Fig. 4 to note is that simulated Northern Hemisphere temperatures and proxy reconstructions exhibit abrupt warming trends beginning in the early twentieth century in all cases except for the natural forcing–only run, Mill_T42_sol_Gao. Unlike the proxies, simulated temperatures and observations initially cool during the industrial period and do not begin warming until the 1920s. From then until the middle of the century, simulated, observed, and proxy temperatures increase by a similar amount. The increase in temperatures near the end of the century is similar between the observations and simulations. Most of the proxy records also show a resumption in warming, although they do not extend as far in time.

Second, simulated temperatures are warmer in the medieval period than afterward. Eight of the proxy records cover both time periods, which we define by years 1000–1200 and 1400–1900, and their average temperature decrease is $-0.17° \pm 0.04°C$ ($p < 0.005$). The simulations produce a slightly stronger temperature decrease, with an average difference of $-0.30° \pm 0.02°C$ ($p < 0.001$) over all the simulations but Mill_T85_all_Crowley, which does not span all of both periods. Causes of the temperature decrease are debated (e.g., Schneider et al. 2009; Servonnat et al. 2010; Miller et al. 2012), but we find it to

be contemporaneous with a slowing down of the AMOC, reduction in the AMO, and increase in North Atlantic sea ice extent in our simulations.

Beyond capturing the decreasing temperature trend, the simulations also capture some of the response to external forcings in the preindustrial millennium. Correlations between annual temperatures from complete proxy records and transient simulations over the years 1100–1850 are on average 0.30 ± 0.03 ($p < 0.001$) prior to smoothing and 0.40 ± 0.02 ($p < 0.001$) after. These correlations are not due to coherence in the internal modes of variability, as there are no significant differences in correlations between simulations of the same resolution versus those of a different resolution, which are initialized from different control simulations. Thus, the simulations are capturing some of the forced temperature response over the preindustrial millennium, particularly on decadal time scales and longer. However, the simulations are not reproducing the proxy temperature responses entirely, as correlations between the simulations are greater than between themselves and the proxies [0.58 ± 0.02 ($p < 0.001$) and 0.827 ± 0.007 ($p < 0.001$) for simulations employing different and the same volcanic forcings, respectively]. Again, resolution makes no difference in the correlations of the simulations with each other, which indicates that these correlation values are not due to coherence in the modes of internal variability. Differences in the responses to external climate forcings may indicate inaccuracies in the forcing datasets, problems with the model's ability to replicate the responses to the forcings, or inaccuracies in the proxy records.

The most noticeable discrepancies between these datasets occur when simulated Northern Hemisphere temperatures exhibit much larger temperature responses to large volcanic events than proxy reconstructions do. These differences yield higher correlations between simulations employing the Crowley et al. (2008) volcanic reconstruction, which has smaller average event magnitudes compared with those employing the Gao et al. (2008) reconstruction (0.36 ± 0.01 and 0.252 ± 0.009, respectively, and difference $p < 0.001$). These simulated temperature responses may be unrealistically large, as other analyses indicate that models exaggerate the climate responses to large volcanic events (Gent et al. 2011; Timmreck et al. 2010). Gent et al. (2011) note excessive global responses in comparison with observations to both the Krakatoa volcanic eruption in 1883 and eruptions in 1902 using CCSM3. Furthermore, Gent et al. (2011) postulate that CCSM3 temperature trends over the industrial period match observations, because overly large volcanic events partially compensate for the lack of inclusion of the indirect effect of aerosols in the model. One reason why CCSM3 may not be modeling large volcanic eruptions accurately is that CAM3 assumes a single particle radius for all volcanic aerosols. It has been shown that in larger volcanic eruptions, the particle radii tend to become larger, thus less radiatively effective, and precipitate out faster than smaller aerosols (Timmreck et al. 2010). Timmreck et al. (2009) showed that by changing the volcanic particle radius, the temperature effects from volcanic eruptions could be changed significantly. Nevertheless, some proxy reconstructions may not be entirely reliable for indicating temperature responses to large volcanic events either. Mann et al. (2012) show that, during very large volcanic events, proxy temperature records based on tree-ring data from near tree lines may not reproduce the strength of the cooling signal and may shift its timing if gaps are introduced into the tree-ring chronology. Only the residual cooling in the years following a year with no tree rings is then detected. Furthermore, Mann et al. (2012) note that volcanic aerosols encourage tree-ring growth by diffusing visible light, which also obscures the reduction in temperatures following a volcanic event.

Thus, the millennium-time-scale simulations reproduce temperature trends and some temperature responses to external forcings in the Northern Hemisphere temperature proxy records. Differences are apparent for large volcanic events, which may indicate both an underestimation in proxy records dependent on tree-ring data and an overestimation of the volcanic response in CCSM3. Next, we present an overview of the characteristics of the simulations' representations of those components of internal climate variability that are expected to possibly influence Greenland climate.

The atmospheric modes of interest we consider include the NAO and the EA, which are defined as the first and second principal components of annual sea level pressure anomalies in the North Atlantic (north of 20°N and within 90°W–30°E). Projections of these modes onto sea level pressures at both T42 and T85 resolutions are provided in Fig. 1. Climatological wind vectors for simulations at each resolution and between 700 and 925 hPa are included for reference. As discussed previously, the NAO is thought to play an important role in regional Greenland climate patterns, because of its influence on the North Atlantic jet. However, Woollings et al. (2010) showed that changes to the eddy-driven North Atlantic jet are not necessarily well described by the NAO alone but by a rotation in NAO − EA phase space. Woollings et al. (2010) demonstrated that in ERA-40 daily data the NAO + EA captures the dominant shifts in jet speed, where a positive (negative) index corresponds to a faster (slower) North Atlantic eddy-driven jet. On the other hand, the NAO − EA axis captures most of

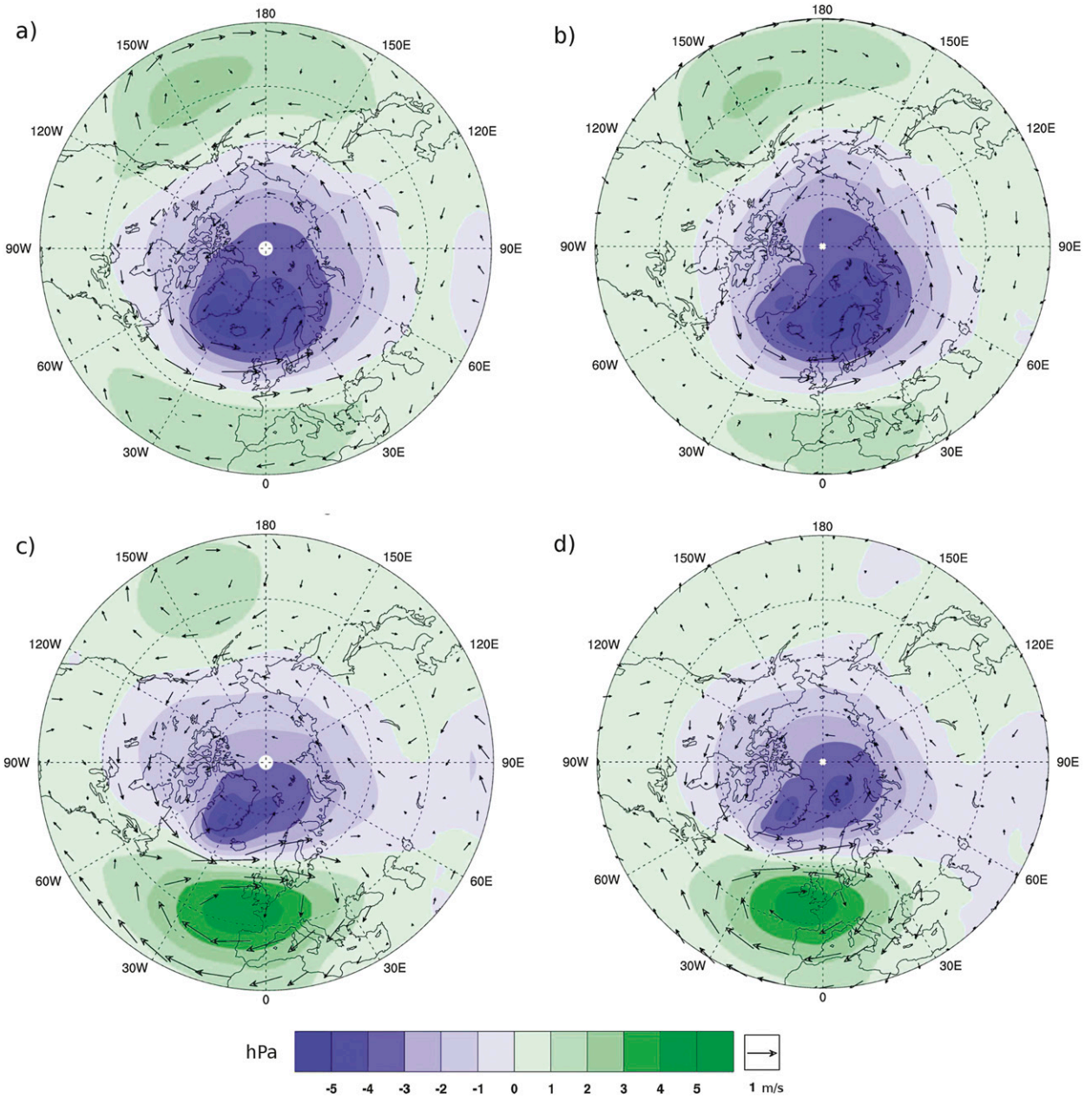

FIG. 5. Projections of the (a),(b) NAO + EA and (c),(d) NAO − EA onto Northern Hemisphere sea level pressures (hPa) for (a),(c) T42 and (b),(d) T85 simulations. Superimposed over these contours are projections of these modes on wind vectors ($m\,s^{-1}$) for DJF from the corresponding simulations.

the variability in jet latitude, where a positive (negative) index indicates a northward (southward) shift of the jet. We projected both the NAO + EA and NAO − EA annual indices onto sea level pressures, and we superimposed the projections of these modes on wind vectors from between 700 and 925 hPa over the contours in Fig. 5. We thereby find that the relationships identified by Woollings et al. (2010) are reproduced in our simulations. The NAO + EA projections primarily involve an increase in the speed of the climatological winds, while the NAO − EA is correlated with a northward shift of the midlatitude jet by approximately 15°. There are noticeable resolution differences in the projections of the NAO + EA and NAO − EA modes in Fig. 5. In both modes, the site of the low pressure center is shifted to the east in the T85 configuration as compared to the T42 configuration. For the NAO − EA, this has the result of splitting the low pressure center into two maxima.

There is no evidence of external forcing of the NAO, the EA or either of their linear combinations in the preindustrial- and industrial-era simulations. Furthermore, the spectra of both the NAO and EA are consistent with white noise processes in the annually averaged data from our millennium simulations. This result is reasonable given that the NAO and EA are understood to be red noise processes with memory time scales on the order of 9–10 days (Casado and Pastor 2012), which is short enough to not be detectable in annual data. Also, Casado and Pastor (2012) show that CCSM3 daily data obtained from the CMIP3 twentieth-century experiment match the ERA-40 data time scales for both the NAO and the EA reasonably well.

We explore next the behavior of North Atlantic sea ice cover over the preindustrial period. North Atlantic sea ice extent is strongly related to both the AMOC and AMO. Thus, we discuss the relationships between these variables after presenting each individually. North Atlantic sea ice cover is defined here by the annually averaged area of monthly sea ice extent enclosed within the 15% concentration limits north of the equator and bounded by 90°W and 90°E. The regions of highest variability in annual sea ice cover in these simulations are first in the Barents Sea, second along the path of the East Greenland Current and around the periphery of the Greenland–Iceland–Norwegian (GIN) seas, and third in the region south of Greenland. Annual sea ice climatologies for all runs are shown in Fig. 6 together with maps of their standard deviations. Annually averaged North Atlantic sea ice extents increase from the twelfth to the sixteenth century and rapidly decrease during the industrial period (Fig. 7a). These trends are not replicated in either control run, which indicates that the increase is a robust response to external forcings during the period. In particular, there are abrupt increases in sea ice extent just following the largest volcanic events, with recoveries on decadal time scales. This prolonged sea ice response to large volcanic events is consistent with previous studies, particularly given that the largest volcanic eruption in 1258 was modeled as a tropical eruption in both volcanic datasets used here (Schneider et al. 2009) and the clustering of large volcanic events during the thirteenth and fifteenth centuries (Miller et al. 2012).

We define the AMOC as the maximum of the annually and longitudinally averaged ocean streamfunction in the Atlantic basin north of 28°N and deeper than 500 m. In the plot of the AMOC maxima time series (Fig. 8a), the first point of note is that the AMOC strength declines gradually to the sixteenth century and increases rapidly at the beginning of the twentieth century in all of the runs. As with sea ice, these trends are not present in either of the control runs over an equivalent period of time following the transient simulation initialization dates. Furthermore, the AMOC decreases are not simply due to coherence in the low-frequency temporal modes across our simulations, because the declines are present in runs at both resolutions, which are initialized from different simulations. Consequently, these AMOC variations are responses to the external forcings, which are all atmospheric in origin.

Second, mean AMOC strength values are the same for transient simulations at both resolutions, but the standard deviations are nearly two times higher in the T42 simulations than the T85 simulations. The AMOC spectra in Fig. 8b show that most of the power in the AMOC time series is on time scales longer than 15 yr for simulations at both resolutions. Standard deviations do not decrease significantly from the control to the transient simulations, so we are not seeing the same suppression in AMOC variability as Bryan et al. (2006) did with the same model. However, the AMOC standard deviations we calculate for the T42 control and transient simulations are 0.71 ± 0.02 Sv ($1\,\text{Sv} \equiv 10^6\,\text{m}^3\,\text{s}^{-1}$) and agree with the control values in Bryan et al. (2006), whereas the T85 values are 0.381 ± 0.007 Sv (difference $p < 0.001$) and are three times smaller than the control values reported in Bryan et al. (2006). Instead, they agree with the low standard deviations of T85 simulations in Bryan et al. (2006) during the recovery from substantial transient forcing. The discrepancies in variability between AMOC maxima in these analyses and those reported in Bryan et al. (2006) may be explained by shifts in the time scales of AMOC variability exhibited by the AMOC maxima time series in their study. Danabasoglu (2008) and d'Orgeville and Peltier (2009b) also find similar shifts in AMOC time scales in their CCSM3 simulations. Our simulations have been run longer than any of these earlier analyses and exhibit consistent power spectra throughout the time series. Thus, their regime shifts may represent changes because of the equilibration process. Nevertheless, the factor of 2 difference in overall AMOC variability between the simulations at T42 and T85 indicate that the simulated AMOC is behaving fundamentally differently at the two resolutions. Given that the ocean and sea ice model resolutions are the same in both cases, it appears that the difference is a result of interactions between the ocean and atmosphere components and possibly through the atmosphere's effects on sea ice. Further analysis of these interactions is beyond the scope of this paper.

Next, the AMO is defined as the difference between Atlantic (80°W–30°E) and global-mean annual sea surface temperature anomalies within 0°–70°N (Deser et al. 2010). The AMO exhibits substantial variability on

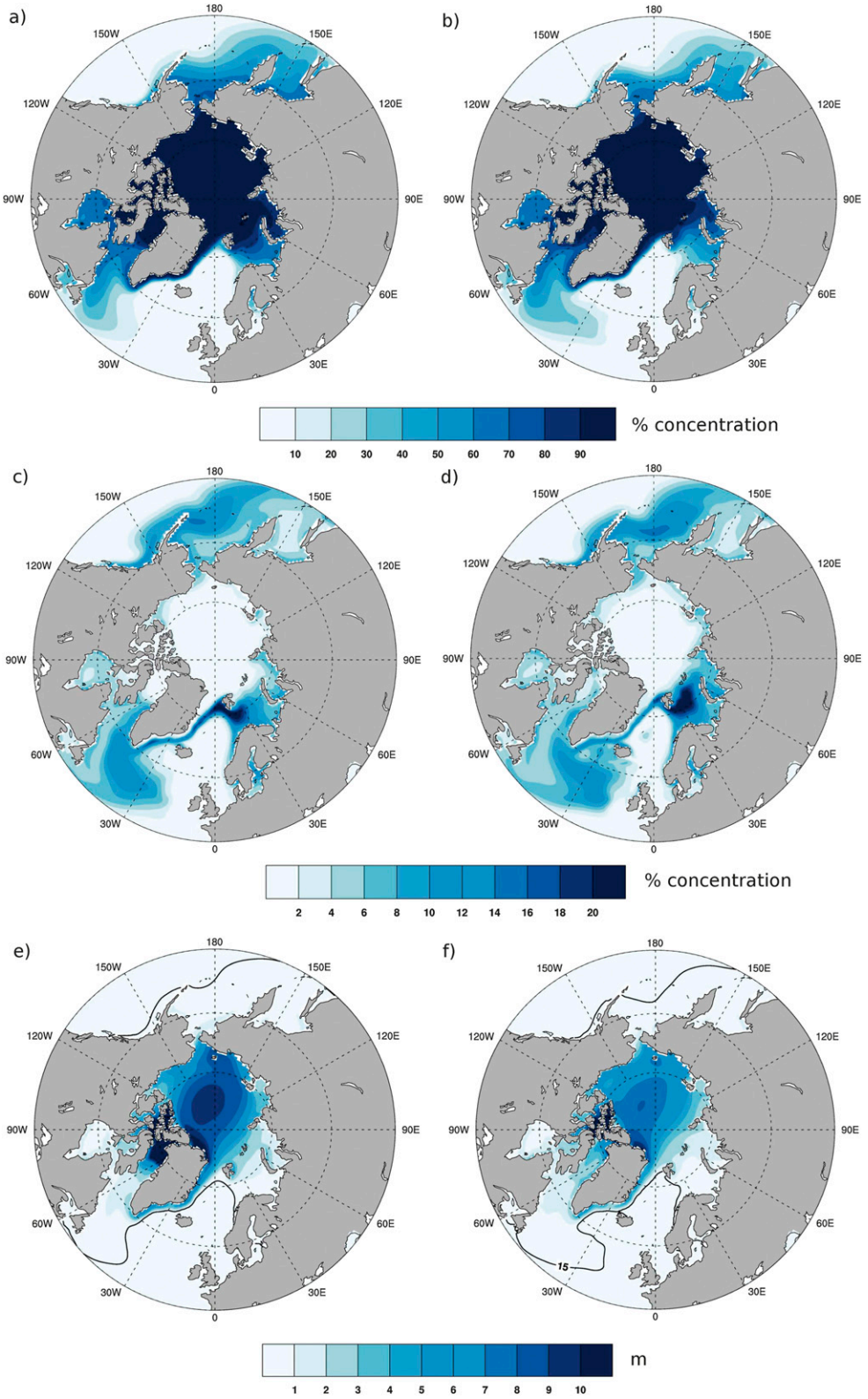

FIG. 6. Annual sea ice concentration climatologies averaged over transient simulations at resolutions of (a) T42 and (b) T85 and (c),(d) corresponding standard deviations. Also, annual sea ice thickness climatologies for (e) T42 and (f) T85 with the 15% concentration contour marked.

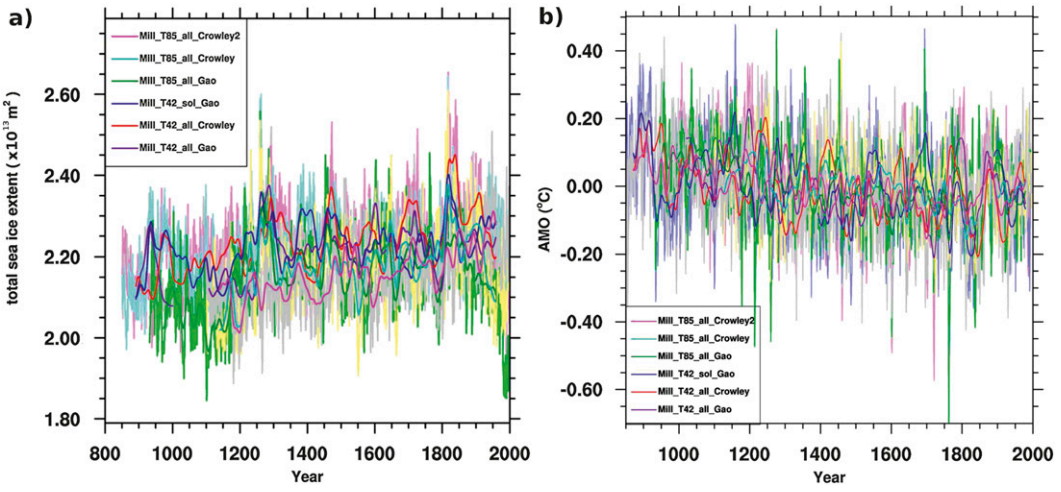

FIG. 7. (a) Sea ice extent within the 15% concentration limits as a function of time for both annual (in light colors) and smoothed data. (b) AMO time series for both annual (in light colors) and smoothed data.

multidecadal and centennial time scales. Figure 7b shows that the AMO decreases in all the transient simulations from the twelfth to the sixteenth century, which is the same period in which North Atlantic sea ice extent increases (Fig. 7a). This decrease is not reproduced in the control runs. There is no increase in the AMO over the industrial period, as may be expected based on increasing Northern Hemisphere temperatures and decreasing North Atlantic sea ice extent. However, this does not imply that North Atlantic sea surface temperatures did not warm over this period, but rather that there were no substantial increases in North Atlantic sea surface temperatures during this period beyond global-mean changes. Instead, there is a consistent increase in the AMO in all simulations in the mid-nineteenth century, with a peak in the 1870s followed by a decrease to the mid-twentieth century. The cause of this pattern is unknown.

As described in the introduction, the NAO, AMO, AMOC, and North Atlantic sea ice extent are understood to be interrelated. We find connections between these variables in our simulations as well, although with stronger correlations in the T42 simulations than in the T85 simulations. The AMO and sea ice

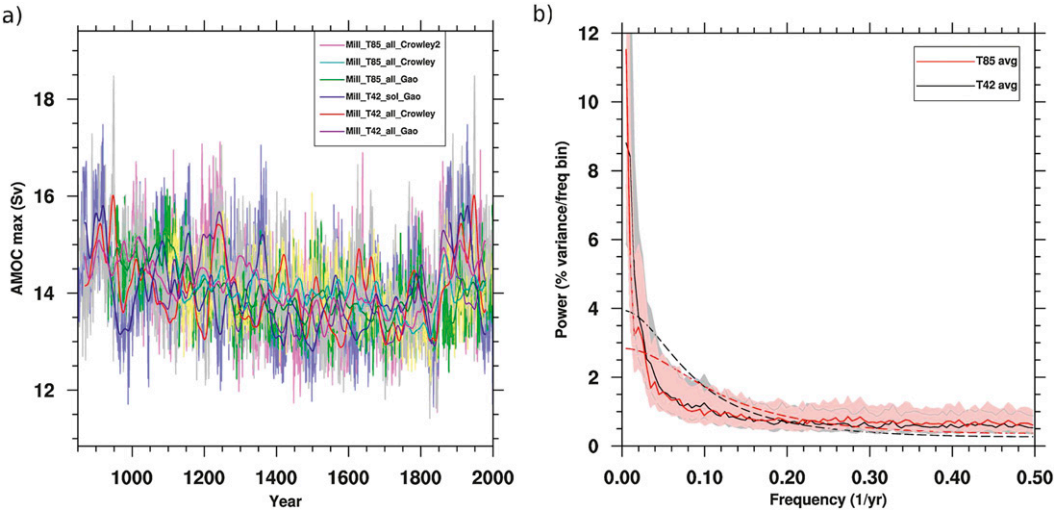

FIG. 8. (a) Time series of the AMOC for all millennium-time-scale simulations. (b) Power spectra of AMOC time series for all runs with an atmospheric resolution of T42 (black) and T85 (red) calculated using Blackman–Tukey methods and a Tukey window truncated at $^1/_5$ the number of data points. Dashed lines indicate the red noise spectra for time series with the same lag-1 autocorrelation coefficients as the data, and shading indicates 95% confidence intervals.

are strongly negatively correlated ($r \sim -0.6$ for T42 and $r \sim -0.5$ for T85) when these variables are either in phase or the AMO lags sea ice by 1 yr. The AMOC lags behind both of them. It is positively correlated with the AMO when it lags by 0–5 yr at values of 0.4 for the T42 simulations and 0.25 for the T85 simulations. Its correlations with sea ice vary more with resolution, as it has its strongest anticorrelations of approximately −0.55 with T42 simulations at lags of 5–7 yr and anticorrelations of −0.25 with T85 simulations at lags of 3–15 yr. Thus, the AMO, AMOC, and sea ice appear to be responding similarly to climate forcings or are influenced by each other, albeit on different time scales.

In the simulations, the AMO, AMOC, and North Atlantic sea ice extent all respond consistently and significantly to solar insolation and the NAO − EA. The AMOC and AMO are strongly positively correlated with low-frequency variations in solar insolation ($r \sim 0.4$ and 0.3, respectively), and sea ice is strongly negatively correlated with them ($r \sim -0.4$). There appears to be a connection between the decreasing orbital contribution and multidecadal total solar irradiance component and the slow variations in these time series over the millennium. The AMO and AMOC (in T85 simulations only) are significantly negatively correlated with the NAO − EA ($r \sim -0.15$ for both) when they lag by 5–15 yr. Sea ice, on the other hand, is significantly positively correlated with the NAO − EA ($r \sim 0.16$) when it lags by 2–7 yr. These correlations with the NAO − EA suggest the presence of a response mechanism as previously described in the introduction of this paper. Other climate indices generate correlations with only subsets of these North Atlantic variables. For example, the AMO and sea ice extent are strongly correlated ($r \sim -0.3$ and 0.3, respectively) with volcanic forcing after a lag of 1 yr. The AMOC does not show any significant relationship with volcanic forcing in our simulations.

The PDO is defined as the first principal component of the difference between sea surface temperature anomalies in the North Pacific (20°–65°N, 120°E–100°W) and global sea surface temperature anomalies (Deser et al. 2010). Analyses of its structure in the CCSM3 model are presented in d'Orgeville and Peltier (2009a). The PDO has very similar characteristics in all our simulations: there is no significant trend in the time series, and the variances are all of similar magnitude. Also, the PDO spectral characteristics illustrated in Fig. 9 are similar at both resolutions and exhibit a large peak in power on a time scale of approximately 13 yr.

Possibly the least likely source of climate variability in Greenland that we consider is that related to ENSO. The ENSO index used in this analysis was defined by sea surface temperature anomalies in the Niño-3.4 region. The annually averaged time series for this index are shown in Fig. 10, with the corresponding 30-yr Gaussian filtered signals superimposed. There is intense variability in the index on annual time scales, and occasional multidecadal excursions from the index mean. The low-frequency shifts to negative ENSO values in Fig. 10 occur in all of the runs and coincide with the largest volcanic events in the forcing time series. Furthermore, the ENSO responses to the 1258 volcanic event are weaker in the runs that were forced by the Crowley et al. (2008) dataset (in red, cyan, and magenta), whose aerosol optical depth values are lower than the values for the same eruption in the Gao et al. (2008) dataset. Although the ENSO time series is shifted in the years following large volcanic events, their values continue to vary at high frequencies with similar amplitudes. This suggests the possibility that these are not actually extended La Niña events but artifacts of the definition of ENSO as anomalies with respect to the local climatology during periods of global sea surface temperature change.

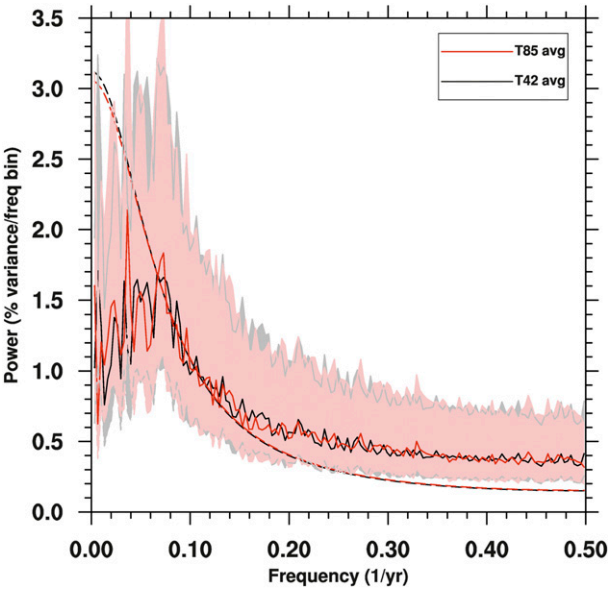

FIG. 9. PDO power spectra for the T42 and T85 simulations calculated using Blackman–Tukey methods and truncating the Tukey window at the number of data points. The 95% confidence limits are in shading, and dashed lines indicate equivalent red noise spectra.

b. *Explaining Greenland's surface climate variability in terms of global climate characteristics*

Greenland temperatures are strongly correlated with Northern Hemisphere temperatures in all the preindustrial simulations and have their highest correlations

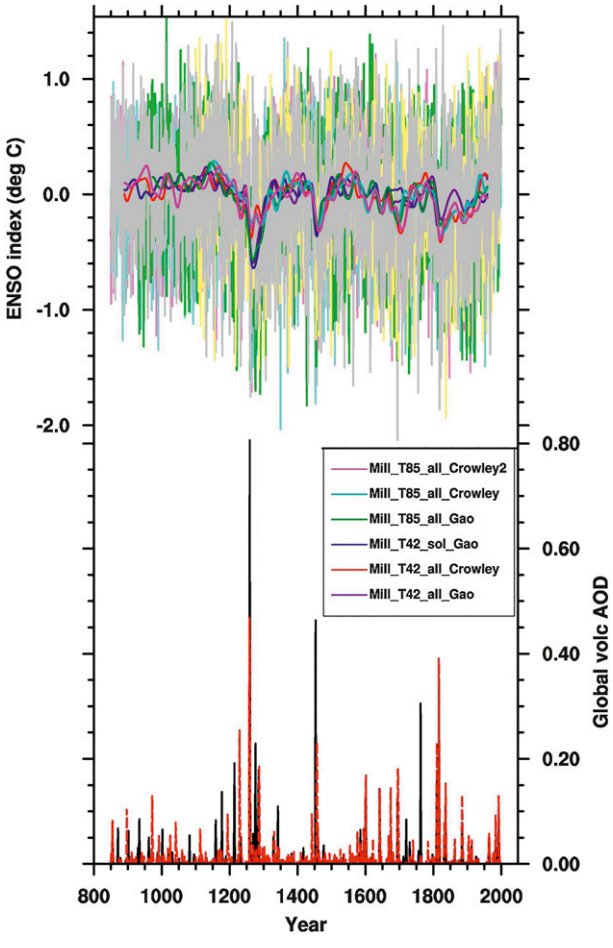

FIG. 10. Annually averaged Niño-3.4 time series for all runs with 30-yr Gaussian averages. Volcanic aerosol optical depths are shown below, with black denoting Gao et al. (2008) and red denoting Crowley et al. (2008).

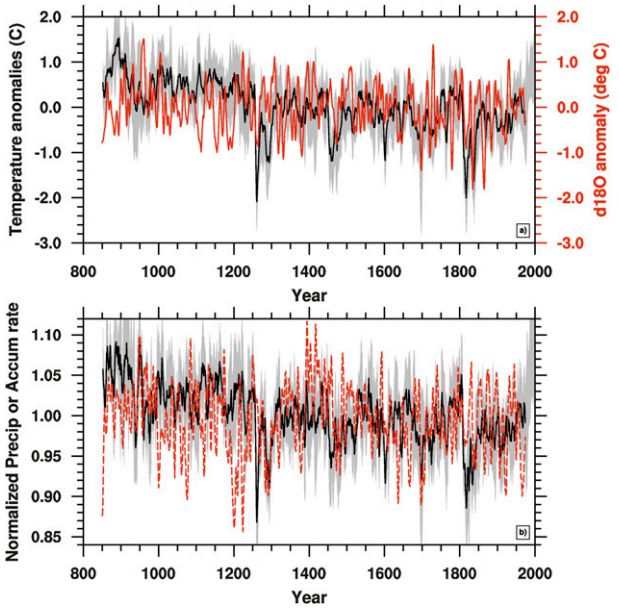

FIG. 11. Time series of simulation ensemble means in black and Andersen et al. (2006) ice core data in red for (a) simulated Greenland average temperatures and $\delta^{18}O$ averaged over three ice cores and (b) normalized annual rates of simulated Greenland average precipitation and Andersen et al. (2006) average accumulation from the same ice cores. Gray shading indicates one standard deviation and all datasets are smoothed by a 5-yr running average.

when they lead by 1 yr ($r = 0.52 \pm 0.01$, $p < 0.001$). In the T42 (T85) control run, however, correlations between Northern Hemisphere and Greenland temperatures are at most 0.3 (0.1), also when Greenland conditions lead the Northern Hemisphere. This suggests that there are similarities in the responses of both Greenland temperatures and the hemispheric average to external forcings in our simulations, although the hemispheric response is slower. Note in Fig. 11 that volcanic events do not appear as anomalous in the Greenland time series as they did in the hemispheric averages. Also, internal climate variability has a larger effect on the regional scale.

Resolution differences are present in the simulated Greenland time series. As with the AMOC, the amplitude of Greenland temperature variability is lower for the high-resolution simulations than the low-resolution runs. The standard deviation in Greenland temperatures is 0.92° ± 0.01°C in the T85 simulations versus 1.17° ± 0.02°C in the T42 simulations (difference $p < 0.001$). Temperature averages also differ, with T85 values 2.5°C ($p < 0.001$) colder than the T42 simulations. As discussed in section 2b, previous analyses indicate that the Arctic is roughly 2°C colder at T42 than T85 because of a stronger low pressure bias in the T85 Arctic climate (deWeaver and Bitz 2006; Hack et al. 2006). Thus, the temperature differences obtained here appear anomalous, even though roughly 1.5°C of this difference can be explained by topography alone. Greenland precipitation rates, on the other hand, are twice as large in the high-resolution simulations compared to the low-resolution simulations, with values of 1.019 ± 0.002 m of water equivalent (mwe) per year deposited over Greenland versus 0.534 ± 0.001 mwe yr^{-1} for the T42 simulations (difference $p <$ 0.001). This is consistent with the higher overall topography at T85 resolution and the sharper topographic gradients present along the coasts of Greenland. Since variance scales with average precipitation (Andersen et al. 2006), we find a corresponding difference in precipitation standard deviations of 0.093 ± 0.001 versus 0.051 ± 0.001 mwe yr^{-1} (difference $p < 0.001$). Consequently, in order to perform comparisons using these time series, we first convert them to anomalies. Greenland

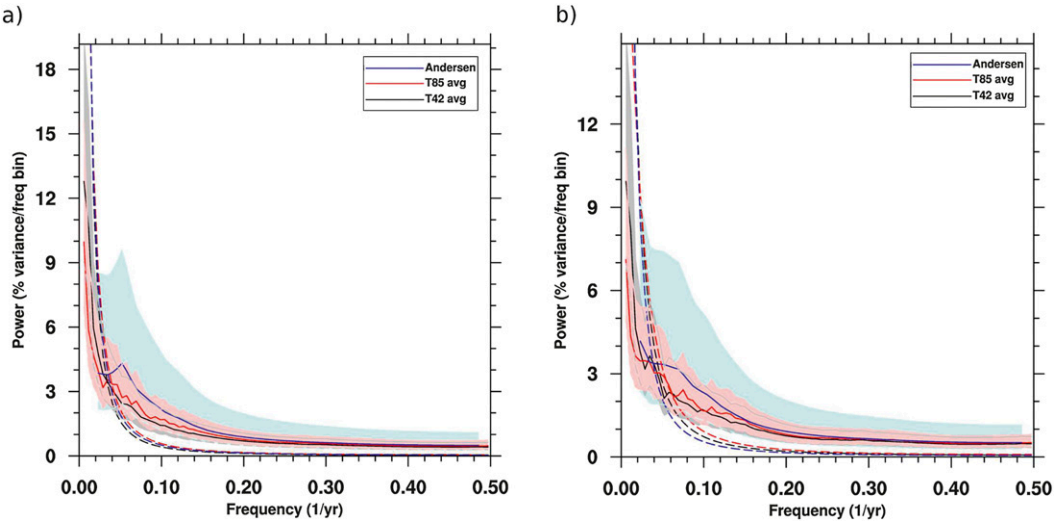

FIG. 12. Comparison between spectra for Andersen et al. (2006) ice records and simulations at resolutions of T42 and T85 for (a) δ^{18}O and temperature and (b) normalized accumulation and Greenland average normalized precipitation. Both datasets have 5-yr running averages applied, and shading indicates 95% confidence intervals. Dashed lines indicate reference red noise spectra for all datasets, given their lag-1 autocorrelation values.

temperature anomalies are defined with respect to averages over years common to all simulations, and precipitation anomaly time series are created by normalizing precipitation rates in each grid cell to their time-average local values and averaging spatially over Greenland.

To assess the accuracy of CCSM3's characterization of Greenland climate over the preindustrial period, temperature and precipitation time series are compared against δ^{18}O and accumulation time series from Andersen et al. (2006) over the years 850–1974. The δ^{18}O record is generated from an average over available years of three historical ice core records [Dye-3, Greenland Ice Core Project (GRIP), and North Greenland Ice Core Project (NGRIP)]. Since the ice core records are obtained from sites only in the interior of the Greenland ice sheet, they do not provide information about temperature or precipitation changes near the ice sheet margins, which are the warmest regions and areas of highest precipitation. Nevertheless, these datasets cover the entire period of our preindustrial simulations and are less susceptible to regional conditions than any one ice core would be, so the comparison is a useful one.

The δ^{18}O provides information about the fractionation processes that occurred from the time moisture was first evaporated from the ocean to its deposition as snow (Sturm et al. 2010). As such, a δ^{18}O chronology only reflects local temperature variations as long as the transport paths and fractionation processes along this trajectory remain the same with time (Sturm et al. 2010). Assuming that this condition is satisfied and that deposition occurs throughout the year, we apply a linear relationship to convert δ^{18}O changes to annual temperatures, $T = (\delta^{18}\text{O} + 13.7\,\text{ppm})$ (Johnsen et al. 1989). Greenland temperature anomalies from the simulations are smoothed with a 5-yr running average to match the Andersen et al. (2006) record and are plotted with it in Fig. 11a. The variance of the δ^{18}O record is 16% lower than that in the T85 simulations and 42% lower than in the T42 simulations. Furthermore, the Greenland temperatures decrease from the medieval period onward, unlike the δ^{18}O record. Consequently, temperature trends for the simulations are an order of magnitude larger than for the ice core δ^{18}O records. Correlations between the Andersen et al. (2006) records and data from our simulations are insignificant, except for the T85 simulations, which are correlated at 0.14 ± 0.03 ($p = 0.05$), and for simulations employing the Crowley et al. (2008) volcanic reconstruction, which are correlated at 0.16 ± 0.04 ($p = 0.05$). It is difficult to ascertain whether these two cases of significance are independent, since more simulations at T85 resolution employ the Crowley et al. (2008) reconstruction. The spectra of Greenland temperatures and δ^{18}O are presented in Fig. 12a. There are no significant differences in spectra between the resolutions or with respect to the Andersen et al. (2006) datasets. Note that the uncertainties in the δ^{18}O spectra are larger since we have only a single dataset.

The accumulation record is extracted from layer thickness data in the same three ice core records by normalizing with respect to mean accumulation rates at each site and applying a statistical model to find

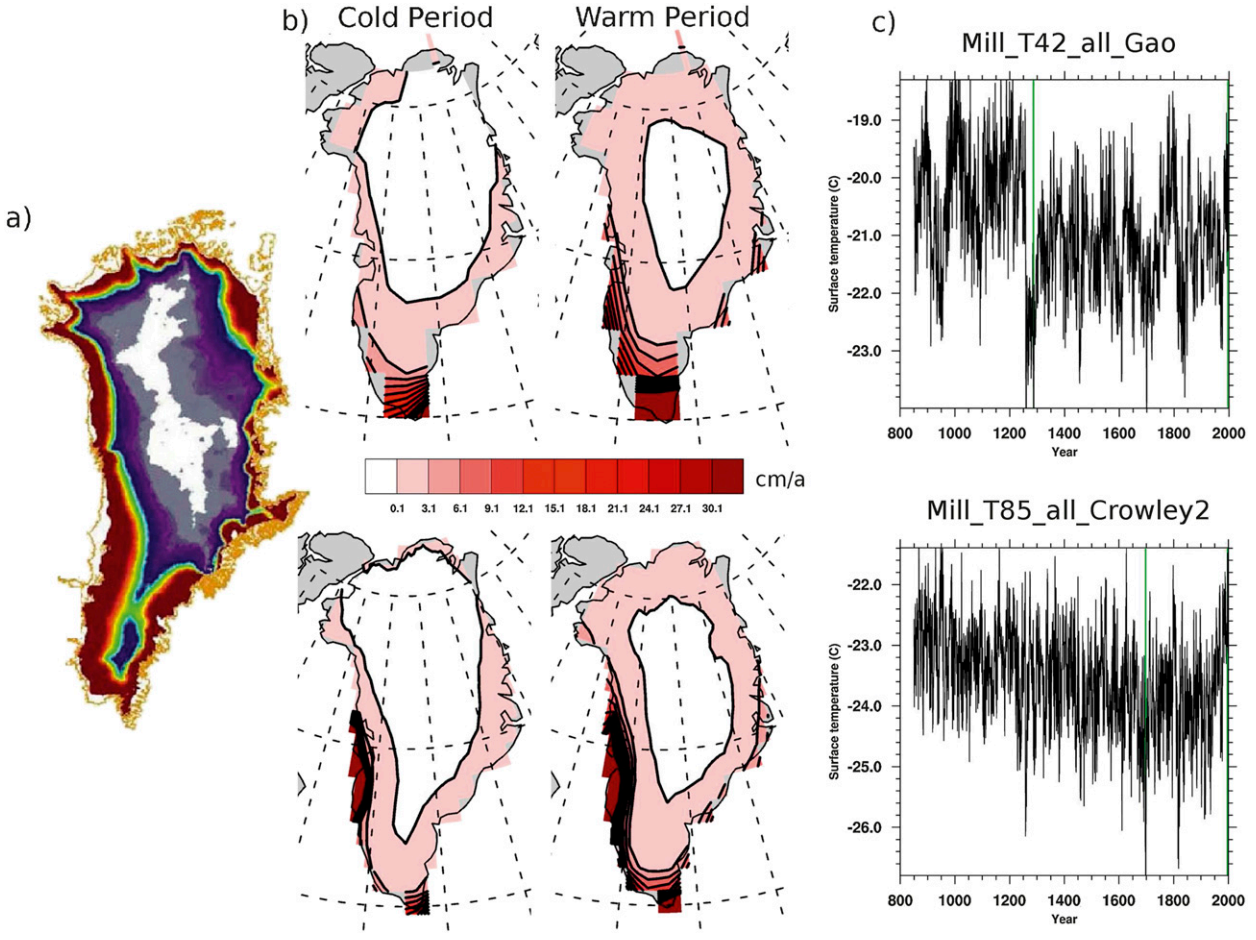

FIG. 13. (a) QuikSCAT map of melt extent over Greenland for the years 2000–04 taken from Wang et al. (2007). Colors represent areas where melt has occurred, while white regions experienced no melt. (b) Model maps of total meltwater production (melted snow) over the melt season [May–October (MJJASO); cm a^{-1}]. The top maps of (b) correspond to Mill_T42_all_Gao, and the bottom maps correspond to Mill_T85_all_Crowley2. (c) Cold years are identified separately for each simulation and are marked by green bars in the Greenland temperature time series, whereas warm years are defined to be the years 1995–99.

a common signal between all the records (Andersen et al. 2006). Accumulation is not solely a measure of precipitation, since it also depends on melt and redistribution processes. However, assuming that these processes are consistent with time under 5-yr smoothing, accumulation variations are a good indication of precipitation changes (Andersen et al. 2006). The comparison with simulated Greenland precipitation is plotted in Fig. 11b. Since the accumulation and precipitation records are normalized locally before averaging, comparing their variances is not very instructive. Furthermore, neither time series exhibits significant trends, and correlations between the two are insignificant. Finally, Fig. 12b shows power spectra for the accumulation and precipitation datasets. There are few resolution differences between the simulated precipitation spectra, and the accumulation spectra also appear consistent within uncertainties.

Although Greenland temperatures and precipitation are uncorrelated with data from Andersen et al. (2006), this does not necessarily indicate that Greenland conditions are especially poorly modeled in these simulations. Internal variability plays a much more important role in regional analyses than hemispheric or global analyses, and no single simulation could be expected to reproduce the exact historical patterns of internal climate variability. However, the fact that there is a stronger correspondence between simulations than between the simulations and the observational records suggests that the simulations exhibit some consistent responses to external forcings that are not matching the ice core reconstructions.

Thus far, our analyses have been based on averages over all of Greenland. It is also useful to compare how well the model is capturing observed regional patterns of temperature and precipitation. Figure 13 shows

extremes in melt extent variability predicted by the model for two runs with different resolution. Surface melt extents are larger in the warm period (1995–99) than the cold period (shown in green bars in Fig. 13c) at both resolutions, and both simulations produce similar melt areas to that from Quick Scatterometer (QuikSCAT) data for the years 2000–04 (Fig. 13a). However, the differences in the distribution of surface melt are as significant between the two resolutions as they are over a given period for either run. The melt area in the T85 run conforms to the coast in a manner more consistent with the QuikSCAT map, and it covers a smaller area overall than in the lower-resolution run, particularly in the south. These features are consistent with differences in orographic heights between the two resolutions as shown in Fig. 3. Melt production extends much farther up the western coast of Greenland in the T85 simulation.

We employ lagged correlation analyses between Greenland temperature and precipitation time series and the modes of variability defined in the previous section to provide context for the regression analyses that follow. Greenland temperatures and precipitation are correlated with each of North Atlantic sea ice, the AMO, and the AMOC such that the relationships between those variables are reproduced. For example, the AMO and AMOC are positively correlated with Greenland temperatures but lag by 2 and 6–11 yr, respectively, whereas sea ice extent is negatively correlated and lags by 1 yr. As a result, including any one of these variables in the regression analysis lagged appropriately is sufficient to describe the relationships to all three. However, we find that when we include any one of them we obscure connections between Greenland conditions and the remaining predictor variables, since the cross correlations with sea ice extent, the AMO, or the AMOC are as significant as the relationships between Greenland conditions and all the remaining predictor variables. Thus, we conclude that Greenland surface climate is responding in concert with North Atlantic sea ice extent, the AMO and AMOC, but we do not include them in the regressions.

The NAO + EA is significantly negatively correlated with Greenland temperatures and precipitation in all of the T85 simulations when the variables are in phase. Relationships with the lower-resolution simulations are less consistent. Correlations with the NAO − EA are similar to those described for the AMO, AMOC, and sea ice. The NAO − EA is significantly negatively correlated with Greenland temperatures when the variables are in phase. In the T85 runs, these correlations are only significant for a single year, but in the T42 simulations the correlations remain significant for temperatures lagging the NAO − EA up to at least a decade. The NAO − EA is only significantly correlated with Greenland precipitation in the T42 runs, with weak positive correlations when the variables are in phase and weak negative correlations for precipitation lagging the NAO − EA for the following 5 yr.

In most transient runs, the PDO shows positive correlations with both Greenland temperatures and precipitation. However, the lag when this positive correlation is maximized is inconsistent between simulations.

Relationships between Greenland temperatures and precipitation and ENSO are only significant over low frequencies, which we showed were responses to volcanic forcing. Consequently, we do not include ENSO in our regression analyses.

Thus, we perform regression analyses of Greenland average annual temperatures and total annual precipitation against volcanic and solar external model forcings and internal modes of variability, including the NAO + EA, NAO − EA, and PDO. The results of the regression analysis on smoothed data are shown in Table 2. Uncertainties in the regression parameters include corrections for autocorrelations in the residuals and are estimated to be at most 0.12 for temperature and 0.15 for precipitation. The regression parameters are plotted with these error bars in Fig. 14. The 95% confidence intervals for the beta values range between 0.17 and 0.24 for temperature and between 0.24 and 0.30 for precipitation.

There are a few ways to test the robustness of these results. Since we have employed two different model resolutions and two different volcanic reconstructions in our mini ensemble, we can first test the consistency of the regression parameters between simulations. This provides insight into the dependence of our results on model configuration and coincidence between the external forcing and internal variability characteristics. The second way we can test the robustness of these results is by splitting each time series into segments and comparing regression values obtained over different sections of the data. Third, we can test the robustness of the regression results by removing predictor variables and seeing how this affects the remaining regression coefficients. Assuming the predictor variables are independent of one another, there should be no effect. This particular suite of variables passes both tolerance and condition-number tests of multicollinearity easily (Sen and Srivastava 1990), so in principle such multicollinearity should not be significantly affecting the results.

On the basis of these analyses, we obtain robust results for solar insolation, volcanic aerosol optical depth, and the NAO − EA, which all are also significantly related to the AMO, AMOC, and North Atlantic sea ice.

TABLE 2. Regression coefficients for millennium simulations.

Response	Simulation	Volcanic	Solar + orbital	NAO + EA	NAO − EA	PDO	R^2
Temperature	Mill_T42_ctl	—	—	0.21	−0.50	0.09	0.36
	Mill_T85_ctl	—	—	0.05	−0.54	0.05	0.29
	Mill_T42_all_Gao	−0.24	0.36	0.06	−0.31	0.20	0.45
	Mill_T42_all_Crowley	−0.25	0.43	0.04	−0.42	0.14	0.60
	Mill_T42_sol_Gao	−0.29	0.26	0.13	−0.51	0.05	0.58
	Mill_T85_all_Gao	−0.42	0.51	−0.09	−0.46	0.15	0.66
	Mill_T85_all_Crowley	−0.46	0.50	0.15	−0.28	0.01	0.70
	Mill_T85_all_Crowley2	−0.29	0.64	−0.17	−0.24	−0.05	0.71
Precipitation	Mill_T42_ctl	—	—	0.15	−0.26	0.07	0.11
	Mill_T85_ctl	—	—	0.10	−0.30	−0.04	0.10
	Mill_T42_all_Gao	−0.23	0.35	0.02	−0.23	0.13	0.33
	Mill_T42_all_Crowley	−0.20	0.43	0.03	−0.30	0.10	0.42
	Mill_T42_sol_Gao	−0.30	0.20	0.10	−0.43	0.03	0.45
	Mill_T85_all_Gao	−0.47	0.37	−0.17	−0.25	0.11	0.44
	Mill_T85_all_Crowley	−0.43	0.38	0.06	−0.12	−0.17	0.40
	Mill_T85_all_Crowley2	−0.20	0.60	−0.14	−0.17	−0.16	0.50

All the runs show consistent and significant positive regression relationships for both Greenland temperatures and precipitation with insolation variability. However, solar regression values decrease in importance for partial regression analyses performed on 500-yr time segments starting after the twelfth century in runs employing the Gao et al. (2008) volcanic dataset (Fig. 15). These differences do not appear to be related to differences in trends in these datasets. Instead, these changes appear to be due to occasional coherence between the volcanic

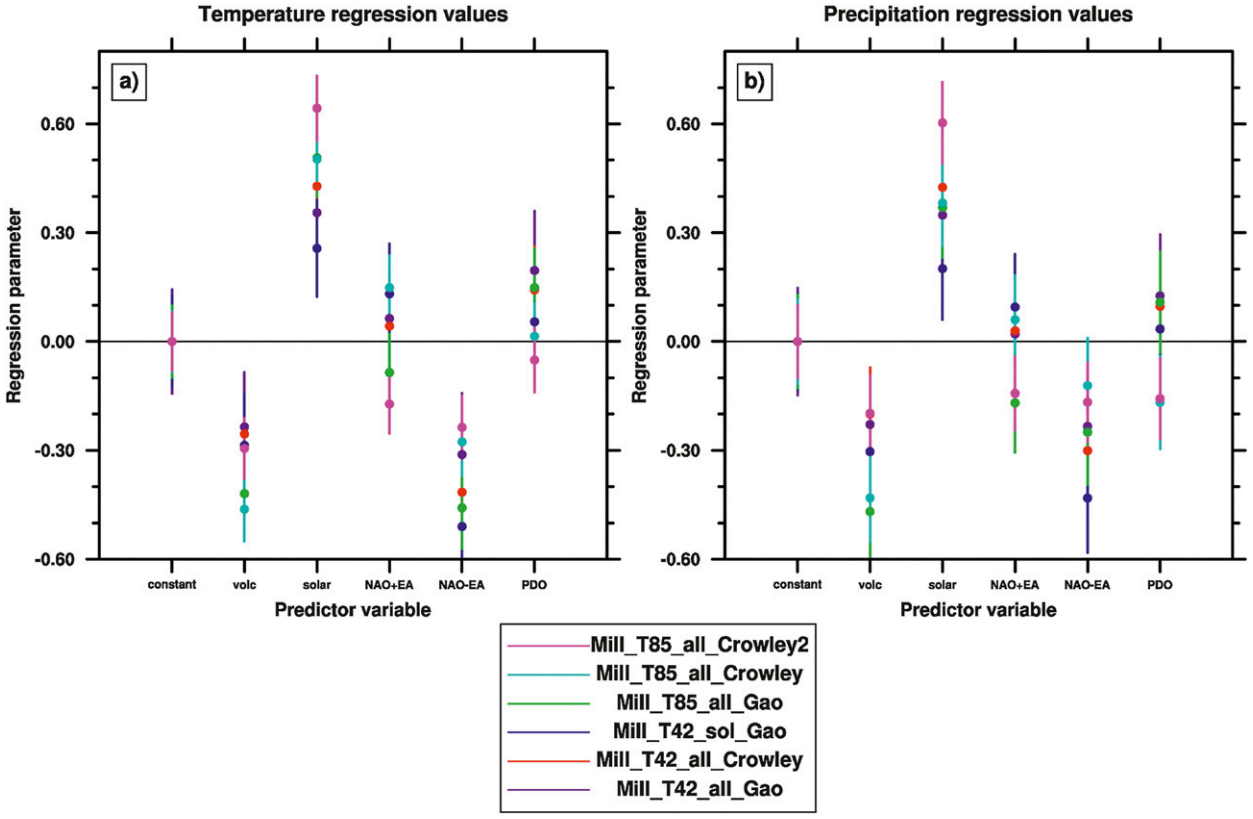

FIG. 14. Regression parameters for the predictor variables listed. Different colors correspond to different simulations. (a) Greenland temperature regressions and (b) Greenland precipitation parameters are shown.

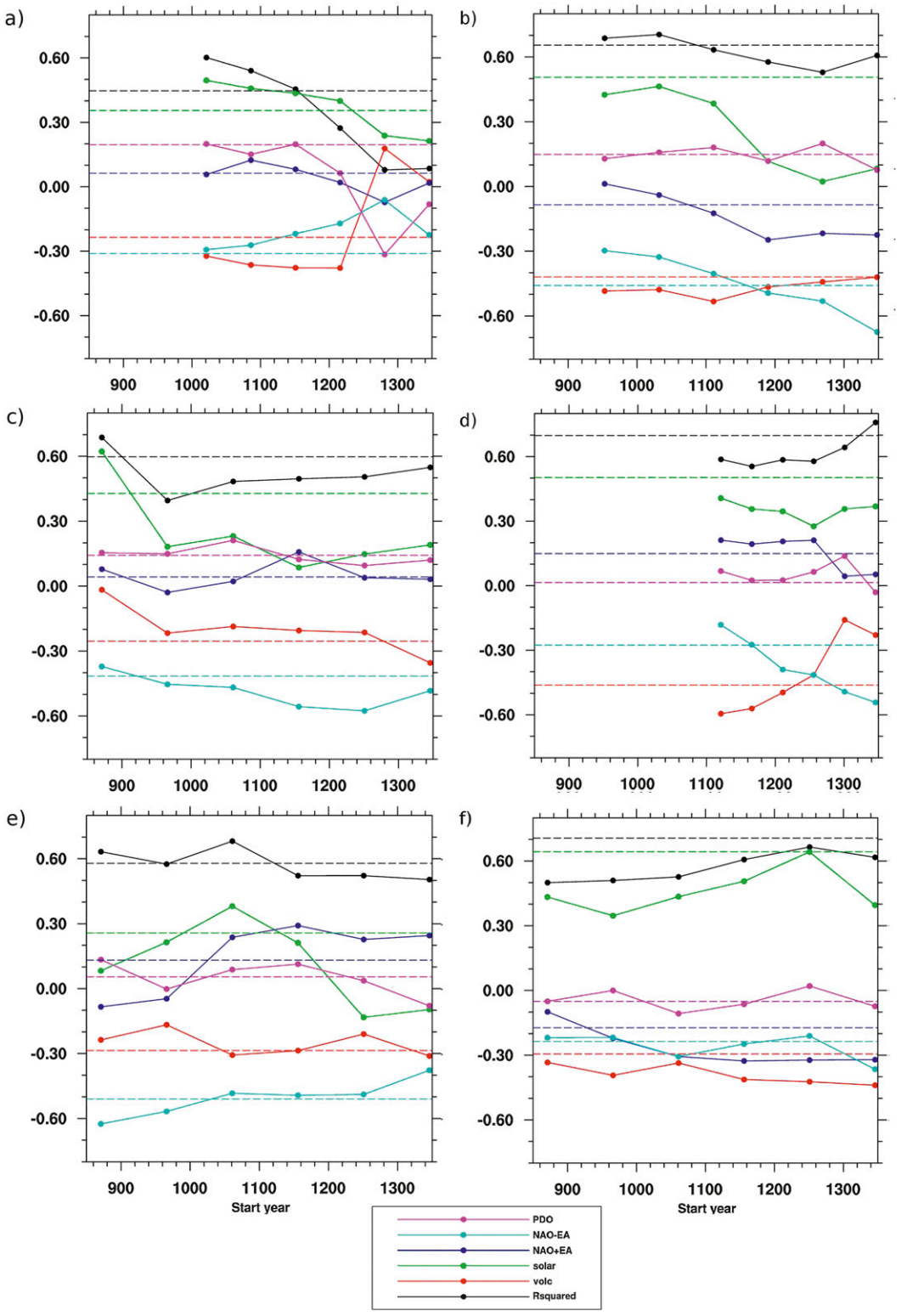

FIG. 15. Regression coefficients obtained with smoothed Greenland temperatures evaluated over successive periods of 500 yr for (a) Mill_T42_all_Gao, (b) Mill_T85_all_Gao, (c) Mill_T42_all_Crowley, (d) Mill_T85_all_Crowley, (e) Mill_T42_sol_Gao, and (f) Mill_T85_all_Crowley2. Regression parameters are plotted as a function of start year in the 850–1850 time period. The fractional variance explained by the regressions over each time segment is plotted in black. Horizontal dashed lines indicate values obtained for the whole period.

aerosol time series and solar insolation. Although these datasets are independent of each other over the entire preindustrial millennium, they are correlated during subsets of that period with values between −0.3 and 0.3 for the Gao et al. (2008) dataset and between −0.5 and 0.3 for the Crowley et al. (2008) dataset. Consequently, the regression parameters over the entire period are more reliable in this case. Overall, the solar regression values are not significantly affected by the removal of other variables from the complete analysis. Thus, we can conclude that there is a significant positive correlation between Greenland temperatures and precipitation and insolation at the top of the model.

We also obtain a robust signal for volcanic forcing, confirming previous work that volcanic events yield lower temperatures over Greenland. We can state further that precipitation is also suppressed in our simulations after a volcanic event, and these effects are sustained for 5–10 yr following the volcanic event. From Fig. 15, we can see that the volcanic regression relations are very consistent with time, with the exception of two runs, Mill_T42_all_Gao and Mill_T85_all_Crowley. These runs show a marked increase in regression parameters following the 1258 volcanic eruptions. One of the peculiarities of the volcanic forcing datasets is that they are dominated by that one extremely large event. It is possible that the response to that one event is affecting volcanic regressions over the entire period, although other simulations do not show a similar sensitivity to it. We also note that the response of Greenland precipitation and temperatures to volcanic forcing is nonlinear, since the short duration of volcanic aerosol loading yields Greenland temperature and precipitation responses for 5–10 yr afterward. Thus, in order to better attribute the volcanic response using a linear model, we may need to fit to a volcanic response fingerprint, which captures such nonlinearities.

As discussed previously, the two North Atlantic atmospheric indices included in the regression analyses represent accelerations (NAO + EA) and shifts (NAO − EA) of the eddy-driven component of the North Atlantic jet. We find that the relationship between the NAO − EA and Greenland temperatures exceeds 95% confidence limits for all the runs. We also show in Fig. 15 that in half of the runs they remain entirely consistent, whereas in the other half they exhibit trends. Negative correlations with the NAO − EA correspond to overall cooling over Greenland when the jet shifts northward, which is consistent with more cold Canadian Arctic air advected over Greenland. As this air holds less moisture, a reduction in precipitation is also consistent. Merely strengthening or weakening the jet does not seem to have much net effect over all of Greenland, however. All the T85 simulations show significant, negative regression parameters with respect to NAO + EA prior to applying the 14-yr Gaussian smoothing. However, after smoothing, the T85 values are inconsistent. The regression parameters for NAO + EA are insignificant with and without smoothing for T42 simulations. Such differences as a function of model resolution may be a result of the sharper topographic coastal gradients in the T85 simulations. Regression maps of the NAO + EA on surface temperatures (not shown) indicate cooling along the west coast of Greenland and a warm tongue along the east coast, which penetrates much farther over Greenland in the T42 simulations. This result is consistent with eddy temperatures during DJF plotted in Fig. 8 of deWeaver and Bitz (2006). Thus, the regression values between the NAO + EA and temperature do not appear to be consistent with time or very strong.

Since we performed our regressions against the NAO combined with the EA, we cannot make direct comparisons with previous studies. However, by examining correlation maps between Greenland temperatures and the NAO in our simulations (not shown), we find that the NAO on its own predicted generally lower temperatures and less precipitation. These results are less consistent between simulations than with the combined NAO and EA modes and are less significant overall. Projections of the NAO on Greenland temperatures in our simulations indicate that responses over Greenland vary significantly by region. Consistent with Fettweis (2007) and Hanna et al. (2013), we see the most negative correlations in the southwest or west and positive correlations in the mideast of Greenland. Precipitation correlation patterns are much more variable between simulations.

Finally, the PDO is not found to be a robust predictor of Greenland temperatures or precipitation. Its regression parameters are insignificant in all the runs and over the entire time series.

Overall, the regressions have been very successful at capturing a significant fraction of the multidecadal variability of Greenland temperatures and precipitation over the past millennium. Consequently, they can be usefully applied as empirical models of Greenland temperatures and precipitation under natural conditions over the industrial period. We obtain volcanic aerosol mass, solar insolation, and internal modes of variability from the industrial simulations to generate estimated Greenland temperature and precipitation time series. We normalize all of these variables with respect to their preindustrial means and standard deviations and apply the regression model. We compare the resulting time series against Greenland conditions derived directly from the model to obtain an estimate of the roles that

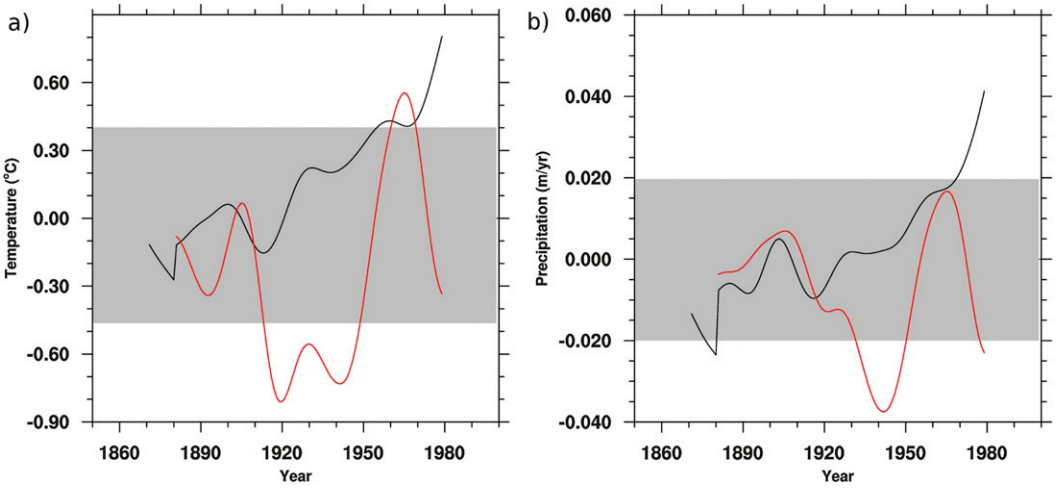

FIG. 16. Average differences between simulated Greenland (a) temperatures or (b) precipitation and those predicted by applying the preindustrial regression model for the fully transient simulations in black. Gray shading encloses 95% confidence intervals for residuals over the preindustrial era. Differences between simulated and regression-predicted (a) temperatures and (b) precipitation from the natural forcing–only run are plotted in red.

anthropogenic greenhouse gases and aerosols play in Greenland surface conditions. In Fig. 16, we plot the average of the differences between empirically predicted and modeled Greenland temperatures and precipitation in black, with gray shading indicating 95% confidence intervals derived from the residuals over the preindustrial period. In red, we plot the differences for the natural forcing–only run, Ind_T42_sol_Gao.

First, we compare how well the empirical regression model predicts conditions over this period for the natural forcing–only run. The empirical estimates do not explain all the variability in this run, with differences varying between 0.6° and −0.8°C while remaining slightly negative on average. In contrast, when we average over all the remaining transient simulations, we can reduce the influence of as yet unexplained variability and extract an anomalous signal in the 1950s. Since that decade, temperatures increase in a way not predicted by the regression model in the average of the full-forcing runs. On the other hand, the Greenland precipitation residuals are consistent with the regression model until the 1970s. Thus, we detect unexplained increases in simulation averages of Greenland temperatures and precipitation in the 1950s and 1970s, respectively. In contrast, we obtain anomalous increases in temperature or precipitation by 1980 in fewer than half of the individual simulations. Thus, these results are consistent with Hanna et al. (2008), who find that historical Greenland temperatures are only significantly associated with Northern Hemisphere temperatures (and thus global warming) after the early 1990s. Instead, Hanna et al. (2008) find Greenland temperatures are mainly associated with NAO variability during the previous several decades. Our results suggest that it may be difficult to isolate comparable temperature and precipitation changes in observed records from Greenland prior to the year 2000.

4. Conclusions

We have generated a suite of fully coupled simulations of the global climate through the periods 850–1850 and 1850–2000 using CCSM3. The six simulations are run with two different resolutions and employ two different volcanic reconstructions. Orbital, total solar irradiance, volcanic, and greenhouse gas forcings are all specified to vary in time over the course of the preindustrial simulations, with the exception of one run in which greenhouse gases are held constant while the remaining forcings varied. We find that global surface temperatures compare well with proxy reconstructions over this period, including the development of a medieval climate anomaly and little ice age. However, the global temperature response to large volcanic events is much stronger than these proxy records would suggest, which is likely a combination of an overamplified response in the model and an underestimation of the effect of these volcanic events in the proxy records.

Using the preindustrial runs, we have explored natural variability in Greenland temperatures and precipitation over the past millennium. This has included the roles of external climate forcings such as volcanic and solar

insolation, as well as internal sources of variability including the NAO, EA, PDO, and ENSO. We have compared the model reconstructions of Greenland temperatures and precipitation against observations compiled from three different ice core records and find that there are no significant correlations between our simulations and the ice core records. The simulations also indicate a decreasing trend in Greenland temperatures over the past millennium that is an order of magnitude larger than in the $\delta^{18}O$ record. On the other hand, simulated precipitation datasets show a similarly small trend as in the Andersen et al. (2006) accumulation dataset. Finally, the spectra from simulated data match spectra from the ice cores within uncertainties. Regionally, resolution makes a big difference to the distribution of surface melt in the simulations, and recent observed melt seasons are similar to those predicted by the model.

We find that Greenland temperatures and precipitation are very highly correlated with North Atlantic sea ice variations (negatively), the AMO (positively), and the AMOC (positively). We find that these climate features all respond similarly and significantly to solar insolation and the NAO − EA and all but the AMOC respond similarly and significantly to volcanic aerosol optical depth, although the timings of their responses vary. We have employed multiple linear regression analysis to extract robust anticorrelations between volcanic forcing and the NAO − EA component of internal variability and Greenland temperatures and precipitation. We also obtain robust positive correlations between solar insolation and Greenland conditions. The connections between other modes of internal variability and Greenland surface conditions tend to be weak or inconsistent, possibly because of their more regional effects. Overall, a linear combination of volcanic aerosol optical depth, solar insolation, NAO + EA, NAO − EA, and PDO is able to describe more than half of the multidecadal variability in Greenland temperatures and at least a third of the multidecadal variability in Greenland precipitation.

Finally, we demonstrate that the regression results derived over the millennium period can be used to extract the influences of anthropogenic greenhouse gases and aerosols over the industrial period. There are significant increases in both Greenland temperatures and precipitation that are not explained by our estimates of natural, background variability in the 1950s and 1970s, respectively.

Acknowledgments. We thank the two anonymous reviewers for their useful feedback. HJA is grateful to her colleagues Dr. I. Simpson, Dr. K. Smith, Dr. P. Hitchcock, and Dr. G. Vettoretti for many helpful discussions. This work was partly funded by the Natural Sciences and Engineering Research Council and the Nuclear Waste Management Organization through the Industrial Postgraduate Scholarship program. Computations were performed on the TCS supercomputer at the SciNet HPC Consortium. SciNet is funded by the Canada Foundation for Innovation under the auspices of Compute Canada; the Government of Ontario; Ontario Research Fund—Research Excellence; and the University of Toronto. The research of WRP at Toronto is funded by NSERC Discovery Grant A9627. Additional funding for this project was provided by NOAA Grant NA110AR4310101. Figure 13a was obtained with permission from L. Wang and John Wiley and Sons under Copyright 2007 by the American Geophysical Union 0148-0227/07/2007JF000760.

APPENDIX

Defining the Regression Model

We applied the following procedure on two runs, Mill_T42_all_Crowley and Mill_T85_all_Crowley, in order to define the regression model employed in these analyses. The choice of variables determined on the basis of these preliminary analyses was then employed with the remaining runs.

First, we optimized the list of climate variables included in the regression analyses. We maximized the coefficient of determination R^2, which represents the proportion of the variance of the original Greenland time series that is captured by all the predictor variables taken together. At the same time, we minimized cross correlations between the predictor variables. To establish significant relationships, we must know that the predictor variables are independent of one another. Otherwise, the regression estimate defined in Eq. (1) has a degree of arbitrariness to it, as adjusting one regression parameter can be compensated for by adjusting the regression parameter of a second, correlated variable.

Second, we tested the residuals under the Gauss–Markov conditions. Meeting the Gauss–Markov conditions ensures that the least squares estimates we take as the regression parameters are good representations of the relationships we are examining (Sen and Srivastava 1990). These conditions are listed below with descriptions of their implications in our analyses:

(i) The expectation value of the residuals should be zero. This suggests two things: first that a linear relationship is a reasonable model of the connection between Greenland climate and the other climate indicators and second that there are no

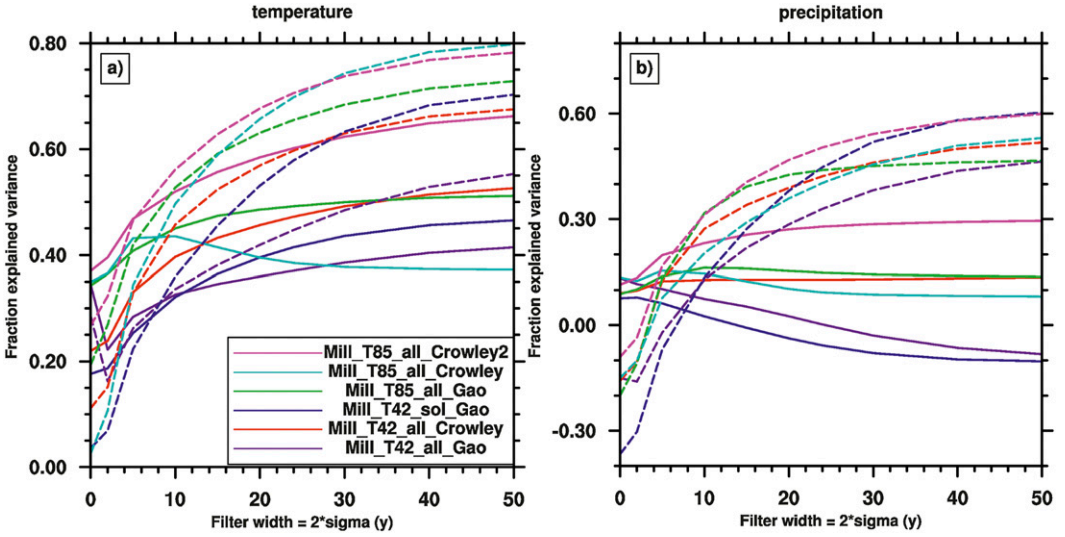

FIG. A1. Percentage of explained variance from (a) temperature and (b) precipitation estimates using regression values generated with unfiltered data (solid lines) and with filtered data (dashed lines). Different colors correspond to different simulations.

important variables missing from the regression model. If a model satisfies this condition, then the relationships between Greenland temperatures or precipitation and other climate fields do not change over the course of the simulations.

(ii) The variance of the residuals is independent of the predictor variables. If this condition is violated, then the regression parameter estimates may not be biased, but their error estimates will not reflect their real uncertainty.

(iii) The residuals are not autocorrelated. This requires that, if there are autocorrelations in the Greenland climate parameters resulting from multidecadal signals, our time series is long enough to adequately resolve these signals and they will be explained by similar features in the predictor variables.

Besides the Gauss–Markov conditions, the regression parameters may also be sensitive to the influence of points far outside the rest of the distribution of values. This is a result of the sensitivity of the ordinary least squares method to differences between large values (Sen and Srivastava 1990). When such points are present, they often are detected in the residuals as violations of the first criterion. We do not have evidence of any such points in the Greenland temperatures or precipitation in Fig. 11.

In our datasets, the third condition was not often met, particularly with Greenland temperatures. Greenland temperatures and precipitation exhibit power at multiple time scales, and not all the low-frequency variability is explained by the list of climate fields used. Thus, the residuals are autocorrelated and not in a way well modeled as an autoregressive process. Consequently, we reduced the effective number of degrees of freedom employed in our estimates of the parameter uncertainties to reflect this limitation.

Third, we examined the regression parameters to see whether they were significantly different than zero. The parameter uncertainties are defined by Eq. (2) (Sen and Srivastava 1990), and we used the general expression from Zwiers and von Storch (1995) to calculate the effective number of degrees of freedom,

$$n_e = \frac{n}{1 + 2\sum_{\tau=1}^{n-1}\left(1 - \frac{\tau}{n}\right)\rho(\tau)}, \quad \text{where}$$

$$\rho(\tau) = \sum_{i=1}^{n-\tau} \frac{(\epsilon_i - \bar{\epsilon})(\epsilon_{i+\tau} - \bar{\epsilon})}{(n - \tau - 1)\sum_{i=1}^{n}\frac{(\epsilon_i - \bar{\epsilon})^2}{n-1}}. \tag{A1}$$

Here, n and n_e represent the original sample size and the equivalent sample size, respectively. The term τ is the lag time, and $\rho(\tau)$ is the autocorrelation parameter in the regression residuals at that lag. We truncated the sum over autocorrelations at the moment that they became negative, since those autocorrelations act to increase our degrees of freedom. Autocorrelation values calculated at large lags are uncertain because of a lack of data in evaluating them, so we could not guarantee that these negative values were not significantly different than 0. This method provides a conservative estimate

of the number of degrees of freedom. If any regression parameters were not significantly different than zero, then we removed those variables and started again.

Fourth, we tested whether it is preferable to apply regression analysis to the datasets directly or to filter them first. To this end, we calculated two sets of regression parameters, one using unfiltered data and the other with data smoothed by a Gaussian filter with a full width at half maximum of 14 yr (i.e., σ of 6 yr). To determine which time scales the two sets of regression parameters effectively capture, we calculated coefficients of determination using each set of regression parameters and datasets smoothed by a succession of Gaussian filters with different widths. Figure A1 shows the R^2 values as a function of dataset filter width for unfiltered regression parameters in solid lines and 14-yr filtered regression parameters in dashed lines. Regression coefficients based on unfiltered datasets explain high-frequency variations in Greenland temperature and precipitation better than regression coefficients obtained from analyses of filtered data. However, they do a poorer job of explaining variations on time scales longer than 5 yr. Since we are most interested in contributions to variability on time scales longer than a decade, we chose to perform our regression calculations using 14-yr smoothed data.

REFERENCES

Alley, R. B., M. K. Spencer, and S. Anandakrishnan, 2007: Ice-sheet mass balance: Assessment, attribution and prognosis. *Ann. Glaciol.,* **46,** 1–7.

——, and Coauthors, 2010: History of the Greenland ice sheet: Paleoclimatic insights. *Quat. Sci. Rev.,* **29,** 1728–1756.

Ammann, C. M., F. Joos, D. S. Schimel, B. L. Otto-Bliesner, and R. A. Tomas, 2007: Solar influence on climate during the past millennium: Results from transient simulations with the NCAR Climate System Model. *Proc. Natl. Acad. Sci. USA,* **104,** 3713–3718.

Andersen, K. K., P. D. Ditlevson, S. O. Rasmussen, H. B. Clausen, B. M. Vinther, S. J. Johnsen, and J. P. Steffensen, 2006: Retrieving a common accumulation record from Greenland ice cores for the past 1800 years. *J. Geophys. Res.,* **111,** D15106, doi:10.1029/2005JD006765.

Berger, A. L., 1978: Long-term variations of daily insolation and quaternary climatic changes. *J. Atmos. Sci.,* **35,** 2362–2367.

Boville, B. A., P. J. Rasch, J. J. Hack, and J. R. McCaa, 2006: Representation of clouds and precipitation process in the Community Atmosphere Model version 3 (CAM3). *J. Climate,* **19,** 2184–2198.

Box, J. E., L. Yang, D. H. Bromwich, and L.-S. Bai, 2009: Greenland ice sheet air temperature variability: 1840–2007. *J. Climate,* **22,** 4029–4049.

Bryan, F. O., G. Danabasoglu, N. Nakashiki, Y. Yoshida, D.-H. Kim, J. Tsutsui, and S. C. Doney, 2006: Response of the North Atlantic thermohaline circulation and ventilation to increasing carbon dioxide in CCSM3. *J. Climate,* **19,** 2382–2397.

Casado, M., and M. Pastor, 2012: Use of variability modes to evaluate AR4 climate models over the Euro-Atlantic region. *Climate Dyn.,* **38,** 225–237.

Chylek, P., M. K. Dubey, and G. Lesins, 2006: Greenland warming of 1920-1930 and 1995-2005. *Geophys. Res. Lett.,* **33,** L11707, doi:10.1029/2006GL026510.

CMIP5, cited 2011: CMIP5: Modeling info: Forcing data. World Climate Research Programme. [Available online at http://cmip-pcmdi.llnl.gov/cmip5/forcing.html.]

Collins, W. D., and Coauthors, 2004: Description of the NCAR Community Atmosphere Model (CAM 3.0). NCAR Tech. Note NCAR/TN-464+STR, 226 pp.

——, and Coauthors, 2006: The Community Climate System Model version 3 (CCSM3). *J. Climate,* **19,** 2122–2143.

Crowley, T. J., 2000: Causes of climate change over the past 1000 years. *Science,* **289,** 270–277.

——, G. Zielinski, B. Vinther, R. Udisti, K. Kreutz, J. Cole-Dai, and E. Castellano, 2008: Volcanism and the little ice age. *PAGES Newsletter,* Vol. 16, PAGES International Project Office, Bern, Switzerland, 22–23.

Danabasoglu, G., 2008: On multidecadal variability of the Atlantic meridional overturning circulation in the Community Climate System Model version 3. *J. Climate,* **21,** 5524–5544.

——, S. G. Yeager, Y.-O. Kwon, J. J. Tribbia, A. S. Phillips, and J. W. Hurrell, 2012: Variability of the Atlantic meridional overturning circulation in CCSM4. *J. Climate,* **25,** 5153–5172.

Delworth, T., and M. Mann, 2000: Observed and simulated multidecadal variability in the Northern Hemisphere. *Climate Dyn.,* **16,** 661–676.

Deser, C., M. A. Alexander, S.-P. Xie, and A. S. Phillips, 2010: Sea surface temperature variability: Patterns and mechanisms. *Annu. Rev. Mar. Sci.,* **2,** 115–143.

deWeaver, E., and C. Bitz, 2006: Atmospheric circulation and its effect on Arctic sea ice in CCSM3 simulations at medium and high resolution. *J. Climate,* **19,** 2415–2436.

d'Orgeville, M., and W. R. Peltier, 2009a: Implications of both statistical equilibrium and global warming simulations with CCSM3. Part I: The decadal variability of the North Pacific basin. *J. Climate,* **22,** 179–199.

——, and ——, 2009b: Implications of both statistical equilibrium and global warming simulations with CCSM3. Part II: On the multidecadal variability in the North Atlantic basin. *J. Climate,* **22,** 5298–5318.

Escudier, R., J. Mignot, and D. Swingedouw, 2013: A 20-year coupled ocean-sea ice-atmosphere variability mode in the North Atlantic in an AOGCM. *Climate Dyn.,* **40,** 619–636.

Fettweis, X., 2007: Reconstruction of the 1979-2006 Greenland ice sheet surface mass balance using the regional climate model MAR. *Cryosphere,* **1,** 21–40.

——, G. Mabille, M. Erpicum, S. Nicolay, and M. Van den Broeke, 2011: The 1958-2009 Greenland ice sheet surface melt and the mid-tropospheric atmospheric circulation. *Climate Dyn.,* **36,** 139–159.

Frank, D., J. Esper, E. Zorita, and R. Wilson, 2010: A noodle, hockey stick, and spaghetti plate: A perspective on high-resolution paleoclimatology. *Wiley Interdiscip. Rev. Climate Change,* **1,** 507–516.

Frauenfeld, O. W., P. C. Knappenberger, and P. J. Michaels, 2011: A reconstruction of annual Greenland ice melt extent, 1784-2009. *J. Geophys. Res.,* **116,** D08104, doi:10.1029/2010JD014918.

Gao, C., A. Robock, and C. Ammann, 2008: Volcanic forcing of climate over the past 1500 years: An improved ice core-based

index for climate models. *J. Geophys. Res.,* **113,** D23111, doi:10.1029/2008JD010239.

Gent, P. R., and Coauthors, 2011: The Community Climate System Model version 4. *J. Climate,* **24,** 4973–4991.

Goosse, H., T. Crowley, E. Zorita, C. Ammann, H. Renssen, and E. Driesschaert, 2005: Modelling the climate of the last millennium: What causes the differences between simulations? *Geophys. Res. Lett.,* **32,** L06710, doi:10.1029/2005GL022368.

Grossmann, I., and P. J. Klotzbach, 2009: A review of North Atlantic modes of natural variability and their driving mechanisms. *J. Geophys. Res.,* **114,** D24107, doi:10.1029/2009JD012728.

Grotjahn, R., L.-L. Pan, and J. Tribbia, 2011: CAM3 biases over the Arctic region during northern winter studied with a linear stationary model. *Climate Dyn.,* **37,** 631–645.

Hack, J. J., J. M. Caron, G. Danabasoglu, K. W. Oleson, C. Bitz, and J. E. Truesdale, 2006: CCSM–CAM3 climate simulation sensitivity to changes in horizontal resolution. *J. Climate,* **19,** 2267–2289.

Hanna, E., P. Huybrechts, I. Janssens, J. Cappelen, K. Steffen, and A. Stephens, 2005: Runoff and mass balance of the Greenland ice sheet: 1958-2003. *J. Geophys. Res.,* **110,** D13108, doi:10.1029/2004JD005641.

——, and Coauthors, 2008: Increased runoff from melt from the Greenland ice sheet: A response to global warming. *J. Climate,* **21,** 331–341.

——, J. Cappelen, X. Fettweis, P. Huybrechts, A. Luckman, and M. Ribergaard, 2009: Hydrologic response of the Greenland ice sheet: The role of oceanographic warming. *Hydrol. Processes,* **23,** 7–30.

——, J. M. Jones, J. Cappelen, S. H. Mernild, L. Wood, K. Steffen, and P. Huybrechts, 2013: The influence of North Atlantic atmospheric and oceanic forcing effects on 1900-2010 Greenland summer climate and ice melt/runoff. *Int. J. Climatol.,* **33,** 826–880.

Hegerl, G., J. Luterbacher, F. Gonzalez-Rouco, S. F. Tett, T. Crowley, and E. Xoplaki, 2011: Influence of human and natural forcing on European seasonal temperatures. *Nat. Geosci.,* **4,** 99–103.

Higgins, M. E., and J. J. Cassano, 2010: Response of Arctic 1000 hPa circulation to changes in horizontal resolution and sea ice forcing in the Community Atmospheric Model. *J. Geophys. Res.,* **115,** D17114, doi:10.1029/2009JD013440.

Holland, M., C. M. Bitz, E. C. Hunke, W. H. Lipscomb, and J. L. Schramm, 2006: Influence of sea ice thickness distribution on polar climate in CCSM3. *J. Climate,* **19,** 2398–2415.

Hurrell, J. W., J. J. Hack, A. S. Phillips, J. Caron, and J. Yin, 2006: The dynamical simulation of the Community Atmosphere Model version 3 (CAM3). *J. Climate,* **19,** 2162–2183.

Jansen, E., and Coauthors, 2007: Palaeoclimate. *Climate Change 2007: The Physical Science Basis,* S. Solomon et al., Eds., Cambridge University Press, 433–498.

Johnsen, S., W. Dansgaard, and J. White, 1989: The origin of Arctic precipitation under present and glacial conditions. *Tellus,* **41B,** 452–468.

Jones, P., D. Lister, T. Osborn, C. Harpham, M. Salmon, and C. Morice, 2012: Hemispheric and large-scale land-surface air temperature variations: An extensive revision and an update to 2010. *J. Geophys. Res.,* **117,** D05127, doi:10.1029/2011JD017139.

Jungclaus, J. H., and Coauthors, 2010: Climate and carbon-cycle variability over the last millennium. *Climate Past,* **6,** 723–737.

Krivova, N., L. Balmaceda, and S. Solanki, 2007: Reconstruction of solar total irradiance since 1700 from the surface magnetic flux. *Astron. Astrophys.,* **467,** 335–346.

Lamarque, J.-F., and Coauthors, 2010: Historical (1850–2000) gridded anthropogenic and biomass burning emissions of reactive gases and aerosols: Methodology and application. *Atmos. Chem. Phys.,* **10,** 7017–7039.

Large, W., and G. Danabasoglu, 2006: Attribution and impacts of upper-ocean biases in CCSM3. *J. Climate,* **19,** 2325–2346.

Mann, M. E., J. D. Fuentes, and S. Rutherford, 2012: Underestimation of volcanic cooling in tree-ring-based reconstructions of hemispheric temperatures. *Nat. Geosci.,* **3,** 202–205.

Masson-Delmotte, V., and Coauthors, 2006: Past and future polar amplification of climate change: Climate model intercomparisons and ice-core constraints. *Climate Dyn.,* **26,** 513–529.

Medhaug, I., and T. Furevik, 2011: North Atlantic 20th century multidecadal variability in coupled climate models: Sea surface temperature and ocean overturning circulation. *Ocean Sci.,* **7,** 389–404.

Meinshausen, M., and Coauthors, 2011: The RCP greenhouse gas concentrations and their extensions from 1765 to 2300. *Climatic Change,* **109,** 213–241.

Miller, K. G., and Coauthors, 2012: High tide of the warm Pliocene: Implications of global sea level for Antarctic deglaciation. *Geology,* **40,** 407–410.

Peltier, W. R., 2009: Closure of the budget of global sea level rise over the GRACE era: The importance and magnitudes of the required corrections for global glacial isostatic adjustment. *Quat. Sci. Rev.,* **28,** 1658–1674.

——, G. Vettoretti, and M. Stastna, 2006: Atlantic meridional overturning and climate response to Arctic Ocean freshening. *Geophys. Res. Lett.,* **33,** L06713, doi:10.1029/2005GL025251.

Schmidt, G., and Coauthors, 2012: Climate forcing reconstructions for use in PMIP simulations of the last millennium (v1.1). *Geosci. Model Dev.,* **5,** 185–191.

Schneider, D. P., C. M. Ammann, B. L. Otto-Bliesner, and D. S. Kaufman, 2009: Climate response to large, high-latitude and low-latitude volcanic eruptions in the Community Climate System Model. *J. Geophys. Res.,* **114,** D15101, doi:10.1029/2008JD011222.

Schoof, C., 2010: Ice-sheet acceleration driven by melt supply variability. *Nature,* **468,** 803–806.

Sen, A., and M. Srivastava, 1990: *Regression Analyses: Theory, Methods, and Applications.* Springer-Verlag, 347 pp.

Servonnat, J., P. Yiou, M. Khodri, D. Swingedouw, and S. Denvil, 2010: Influence of solar variability, CO_2 and orbital forcing between 1000 and 1850 AD in the IPSLCM4 model. *Climate Past,* **6,** 445–460.

Shepherd, A., and Coauthors, 2012: A reconciled estimate of ice-sheet mass balance. *Science,* **338,** 1183–1189.

Small, C., and R. J. Nicholls, 2003: A global analysis of human settlement in coastal zones. *J. Coastal Res.,* **19,** 584–599.

Stroeve, J., M. M. Holland, W. Meier, T. Scambos, and M. Serreze, 2007: Arctic sea ice decline: Faster than forecast. *Geophys. Res. Lett.,* **34,** L09501, doi:10.1029/2007GL029703.

Sturm, C., Q. Zhang, and D. Noone, 2010: An introduction to stable water isotopes in climate models: Benefits of forward proxy modelling for paleoclimatology. *Climate Past,* **6,** 115–129.

Swingedouw, D., L. Terray, C. Cassou, A. Voldoire, D. Salas-Melia, and J. Servonnat, 2011: Natural forcing of climate

during the last millennium: Fingerprint of solar variability. *Climate Dyn.,* **36,** 1349–1364.

——, J. Mignot, S. Labetoulle, E. Guilyardi, and G. Madec, 2013: Initialisation and predictability of the AMOC over the last 50 years in a climate model. *Climate Dyn.,* **40,** 2381–2399.

Tarasov, L., and W. R. Peltier, 2005: Arctic freshwater forcing of the Younger-Dryas cold reversal. *Nature,* **435,** 662–666.

Tett, S. F., and Coauthors, 2007: The impact of natural and anthropogenic forcings on climate and hydrology since 1550. *Climate Dyn.,* **28,** 3–34.

Timmreck, C., S. Lorenz, T. Crowley, S. Kinne, T. Raddatz, M. Thomas, and J. Jungclaus, 2009: Limited temperature response to the very large ad 1258 volcanic eruption. *Geophys. Res. Lett.,* **36,** L21708, doi:10.1029/2009GL040083.

——, H.-F. Graf, S. Lorenz, U. Niemeier, D. Zanchettin, D. Matei, J. Jungclaus, and T. Crowley, 2010: Aerosol size confines climate response to volcanic super-eruptions. *Geophys. Res. Lett.,* **37,** L24705, doi:10.1029/2010GL045464.

van den Broeke, M., and Coauthors, 2009: Partitioning recent Greenland mass loss. *Science,* **326,** 984–986.

Velicogna, I., and J. Wahr, 2006: Measurements of time-variable gravity show mass loss in Antarctica. *Science,* **311,** 1754–1756.

Vieira, L. E., S. K. Solanki, N. A. Krivova, and I. Usoskin, 2011: Evolution of the solar irradiance during the Holocene. *Astron. Astrophys.,* **531,** A6, doi:10.1051/0004-6361/201015843.

Wake, L., P. Huybrechts, J. Box, E. Hanna, I. Janssens, and G. Milne, 2009: Surface mass-balance changes of the Greenland ice sheet since 1866. *Ann. Glaciol.,* **50,** 178–184.

Wang, L., M. Sharp, B. Rivard, and K. Steffen, 2007: Melt season duration and ice layer formation on the Greenland ice sheet, 2000–2004. *J. Geophys. Res.,* **112,** F04013, doi:10.1029/2007JF000760.

Woollings, T., A. Hannachi, and B. Hoskins, 2010: Variability of the North Atlantic eddy-driven jet stream. *Quart. J. Roy. Meteor. Soc.,* **136,** 856–868.

Yang, J., W. R. Peltier, and Y. Hu, 2012a: The initiation of modern ''soft snowball'' and ''hard snowball'' climates in CCSM3. Part I: The influences of solar luminosity, CO_2 concentration, and sea ice/snow albedo parameterizations. *J. Climate,* **25,** 2711–2736.

——, ——, and ——, 2012b: The initiation of modern ''soft snowball'' and ''hard snowball'' climates in CCSM3. Part II: Climate dynamical feedbacks. *J. Climate,* **25,** 2737–2754.

Zwiers, F. W., and H. von Storch, 1995: Taking serial correlation into account in tests of the mean. *J. Climate,* **8,** 336–351.